Interface Investigation of Horizontal Core-Annular Flow

Kangjun Jia

Master of Science Thesis

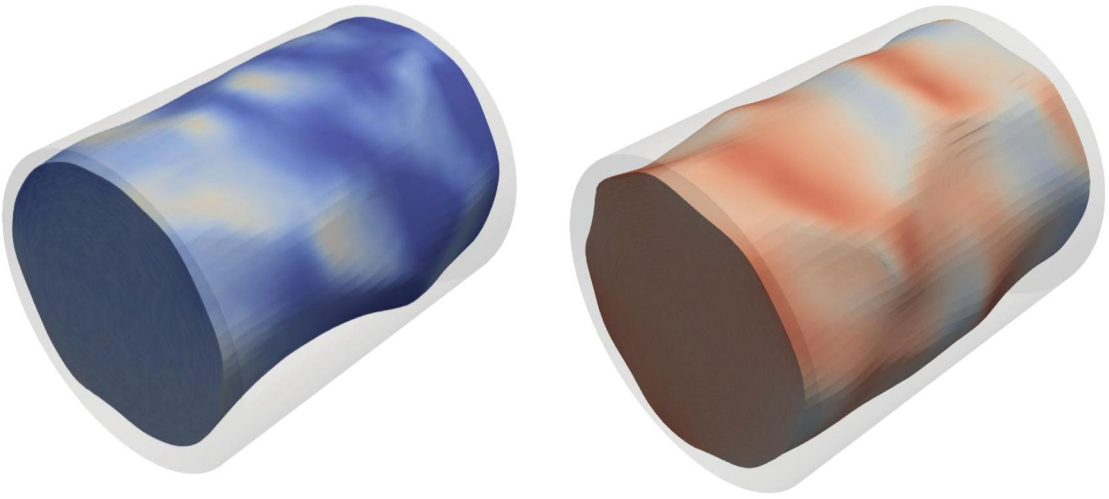

TU Delft Delft University of Technology

Process and Energy

P&E report number 2930

Interface Investigation of Horizontal Core-Annular Flow

Master of Science Thesis

For the degree of Master of Science in Mechanical Engineering at Delft University of Technology

Kangjun Jia

November 14, 2018

Faculty of Mechanical, Maritime and Materials Engineering (3mE) · Delft University of Technology

Abstract

The transport of highly-viscous oil in the core-annular flow regime in a horizontal pipe is investigated with a numerical simulation study. In this flow type the viscous oil is lubricated by a water annulus along the pipe wall. The Launder-Sharma low-Reynolds number $k - \epsilon$ turbulence model is used with the Volume-of-Fluid solver in interFOAM. Three types of simulations were carried out: 3D multiphase flow in a pipe section, 2D multiphase flow in an axi-symmetric pipe section (wedge-shaped section), in which gravity is ignored, and 2D single phase water flow in the annulus, using an imposed wavy boundary. This enabled to study the effect of the viscous oil core on the annulus behaviour, such as the turbulence structures and possible dispersion of oil into the water annulus. In particular the rationale of a 'solid-core' assumption is discussed through the comparison between simulations for the annulus that use the 'interface-bounded' flow and 'wall-bounded' flow.

A main finding of this study is that the use of the Compressive Volume of Fluid (CVOF) method in the multiphase simulations gives spurious dispersion of oil in the water annulus. This is the primary cause of the over-prediction of the pressure gradient simulations carried out in a previous study. Therefore, the Coupled Level-Set Volume of Fluid (CLSVOF) interface capturing method has been implemented in the 3D multiphase model. The new predictions show a good agreement with the experimental data at 20, 30, 40 °C (corresponding to a descrease in the oil viscosity). The oil dispersion in the annulus region close to the wall is diminished by using the new method while the sharpness of the interface is not improved. The CLSVOF interface capturing method is concluded to be an efficient and reliable interface capturing method for the numerical prediction of core-annular flow.

Table of Contents

List of Figures

List of Tables

Acknowledgements

Core-annular flow is indeed an interesting topic including the application of turbulence, numerics and experiments. Working on this topic has been really a precious experience for me to master many aspects of fluid dynamics.

I would like to share my sincere thanks to my supervisors Prof. dr. ir. Ruud Henkes and Prof. dr. ir. Gijs Ooms for the guidance on the theoretical analysis and during the writing of the thesis. I also want to express my gratitude to Dr. ir. Mathieu Pourquie for the discussions on the numerical simulations, and also for the jokes during the coffee breaks.

I would like to thank Dr. ir. Wim Paul Breugem for the introduction of the Coupled Level Set and Volume of Fluid Method during the lunch talk. Without your enlightening presentation I would not have found the influence of the interface capturing method. Finally, I would like to thank my parents, and all the people who have helped and supported me throughout my thesis project.

Delft, University of Technology — Kangjun Jia
November 14, 2018

Chapter 1

Introduction

The global production of crude oil is becoming more difficult as the resources of conventional crude oil are depleting. Therefore also the production of heavy crude oil is considered by the oil and gas industry (Ismail et al., 2015). For the purpose of transporting the highly-viscous oil efficiently, the water-lubricated technique has been found to significantly decrease the required pressure gradient. Thus, this technique has generated much interest, and over the years various studies were carried out in pipelines, both with experiments and through numerical simulations. In this application, which is the so-called core-annular flow (CAF), a flow pattern is formed in which highly-viscous oil flows in the pipe core region, whereas water, with its low viscosity, flows in the annulus around the oil core. Since the pumping pressure is balanced by the wall-shear stress, due to the water film flow along the pipe wall, the lubricated flow only requires a pressure as needed to drive the water alone at the same throughput, independent of the viscosity of the oil (Joseph et al., 1997). Therefore, the lower pressure drop and lower energy consumption can be established with this type of flow pattern.

The core annular flow is one of the flow patterns that can be observed in the two-phase flow through pipelines. Due to the large liquid/liquid momentum transfer the relatively small buoyancy effects, the structure of the oil/water system is quite different from that of the gas/liquid system. Generally, the flow pattern of an oil/water system can be identified into three main types: stratified flow, core-annular flow and dispersed flow, shown in figure 1-1. Other flow regimes, like stratified flow with some mixing at the interface, are classified as a transition status between the three types.

The transition between flow patterns is highly dependent on the volume fraction of the water (which is typically in the range of 10-30 % for CAF(Saniere et al., 2004)), and on the stability of the oil/water interface. It was reported by Joseph et al. (1984) that, through applying the linear instability analysis that the less-viscous fluid always tends to lubricate the wall in a concentric configuration with waves generated between the two phases in a circular pipe, due to the viscous dissipation principle. The presence of waves at the water/oil interface will generate a specific pressure variation in the annular layer, resulting in a counterbalance force of the buoyancy effect to the core in a horizontal pipe (Ooms et al., 2007). This phenomenon

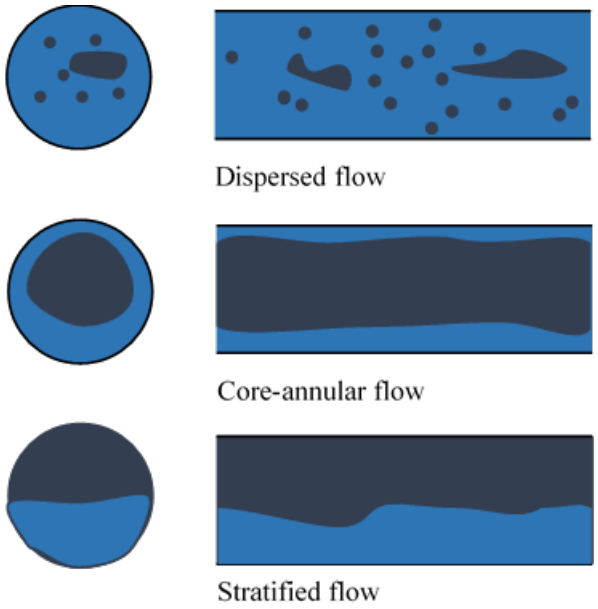

Figure 1-1: Basic flow patterns of the oil/water system in a horizontal pipe, dark blue represents the oil phase,and light blue represents the water phase

provides the possibility to prevent that oil (despite its lower density than that of water) touches and fouls the pipe wall in a horizontal pipe.

Based on the theoretical analysis, various numerical simulations have been carried out to investigate the core-annular flow in detail. Bai et al. (1996) carried out a Direct Numerical Simulation (DNS) for the spatially periodic wavy core flow under the assumption of a rigid moving oil core and asymmetrically distributed waves. The simulation showed a good agreement with the experimental data obtained by Bai et al. (1992) for the upward flow in a vertical pipe. During the simulations, they also found a positive high pressure region at the wave front, where the water enters into the wave. It was suggested that the pressure force in this region, which is exerted on the core, is required to levitate the core off the wall when the densities of the water and oil are different. Following this conjecture, Li and Renardy (1999) improved the simulations by relaxing the axisymmetric assumption, allowing to study the effect of the density difference between the two fluids. The simulation predicted the Reynolds-number-related bamboo waves, which reduce the wave length and steepen the peaks as the Reynolds number increases. The vortex that occurs near the wave crests in the upward flow gives induces a minimum pressure region, whereas the position of the vortex differs in the downward flow with bamboo waves as the result of the buoyancy force direction. Subsequent research on interpreting the levitation of the core for the flow with a density difference between the liquids has been carried out by Ooms et al. (2013) in the horizontal pipe, while using a soft oil core. It was concluded that the core levitation at a high Reynolds number is caused by the inertial forces, whereas at a low Reynolds number viscous (lubrication) forces are responsible for the levitation. The flow behaviour at high Reynolds numbers will be investigated with 3D non-axisymmetric simulations in this thesis.

Apart from the levitation theory, the research efforts have also focused on the turbulence in

the water annulus. Ko et al. (2002) applied the shear stress transport(SST) k-ω model onto the horizontal core-annular flow and compared the results with and without it. It is found that the waves become shorter and steeper when the turbulence model is applied. The flow with a turbulence model also shows better agreement with the experimental data than the flow with a laminar approach. Furthermore, Ingen Housz et al. (2017) and Konings (2017) started to use the open source code OpenFOAM and employed the Volume of Fluid method with an alternative turbulence model in the simulation. The Launder-Sharma $k-\epsilon$ model was also concluded to be a valid turbulence model for the prediction of the pressure drop of the flow, similar to the SST k-ω model. However, there is an under-prediction by 15% at a relatively low temperature of $T = 20\,^{\circ}\mathrm{C}$ (which gives an oil viscosity of 3338 cSt), and the simulations largely over-predicted the pressure drop by 150% at $T = 40\,^{\circ}\mathrm{C}$ (which gives an oil viscosity of 718 cSt). Recommendations were made to modify the turbulence model close to the interface in the annulus.

While earlier studies considered a moving solid core (Bai et al., 1996; Ko et al., 2002; Ooms et al., 2007), later also the interface capturing method for an oil core with a finite viscosity was included. Most of the previous studies, like (Ooms et al., 2013; Beerens et al., 2014; Ingen Housz et al., 2017; Shi et al., 2017), applied the Volume of Fluid (VOF) method to capture the oil/water interface for the mass conservation. Recently, Kim and Choi (2018) used DNS with the Level-Set (LS) method for different oil holdups; their results show a good agreement with the VOF-RANS simulation (Ko et al., 2002; Ingen Housz et al., 2017). Here the mass conservation was obtained by calculating the volume fraction from the linearizd level-set function(Van Der Pijl, A. Segal, C. Vuik and P. Wesseling, 2005). The application of the Level Set function is beneficial, because it gives a good robustness in the interface reconstruction under severe topology changes, which is also a promising approach for the proper representation of the turbulent-wavy interface.

1-1 Research proposal and method

For a given flow rate, a large over-prediction of the pressure gradient with a fixed total flow rate and hold-up ratio at high temperatures (i.e. reduced oil viscosities) in a horizontal pipe was found in the previous simulations carried out by Konings (2017). In an effort to improve the predictions, our research has specific attention for the flow in the water annulus. Not only the turbulence predicted by the turbulence model is investigated, but also the numerical accuracy of the oil/water interface reconstruction. Simulations are carried out in the open source library, OpenFOAM, with the Launder-Sharma $k-\epsilon$ turbulence model. The Coupled Level Set and Volume of Fluid (CLSVOF) interface capturing method is implemented and incorporated into the multiphase transient solver, interFOAM, instead of using the default method, which is the VOF method with the compressive scheme. Furthermore, to obtain shorter computer times, parallel calculations are performed in the Open-MPI library,in which the model is divided into several sub-domains.

1-2 Research outline

In this thesis, the "solid-core" assumption is investigated through comparing simulations for oil with a finite viscosity with simulations that use a fixed wavy interface on a solid moving wall in Chapter 4. Simulations are carried out with a 2D wedge-shaped multiphase model and with a 2D wavy-shaped single-phase model, both using the Launder-Sharma $k-\epsilon$ turbulence model. Chapter 2 summarizes the basic concept and the primary dimensionless numbers utilized in the simulation. In Chapter 3, the new interface capturing method, which is the Coupled Level Set and Volume of Fluid (CLSVOF) approach, is introduced. The results are compared with results obtained with the compressive scheme in the VOF method (CVOF). It is found that there is numerical dispersion of oil droplets in the water annulus when the CVOF method is applied at high temperatures(low oil viscosities) in Chapter 5. The CLSVOF method is then applied for the same conditions in the 3D horizontal pipe model to alleviate the oil dispersion and to sharpen the phase interface. Then a convergence study is performed based on the 2D wedge-shaped model using the CLSVOF method, with the purpose of checking consistency with the linear stability theory. Finally, conclusions and recommendations are given in Chapter 6.

Chapter 2

Multiphase flow

The multiphase flow in pipelines has been extensively investigated in industry and in academia. Here the term "multiphase" refers to the combination of more than 2 of the gas/liquid/solid phases,e.g., air/water/particle phases in a gas-lift system and water/oil phases in water-lubricated oil transport. We focus on the oil/water flow in a pipe. Here there are two incompressible, immiscible Newtonian liquids, with a surface tension at the interface and with a density difference. The water-lubricated transport technique has the advantage that there is a core-annular flow pattern, in which the low viscosity of the water, that wets the full pipe perimeter, reduces the pressure drop. In this chapter we will discuss the basic features of multiphase flow, which can be used in the research on the numerical method.

2-1 Flow parameters

Figure 1-1 shows that the oil/water flow in horizontal pipe can be characterized by three main types: dispersed flow, core-annular flow, and stratified flow. In the core-annular flow, due to the lower density of the oil than that of the water, the core has the tendency to ascend and touch the top wall of the pipe, making this flow pattern hard to maintain. The transition of the flow pattern is highly dependent on the parameters such as the superficial velocity of each phase, the pipe diameter, the density difference, the surface tension and the inclination of the pipe. However, the definitions of the flow patterns have not been standardized and the restrictions differ from case to case. The following equations introduce several primary parameters utilized in the oil/water system:

$$U_o = Q_o/A, U_w = Q_o/A, \tag{2-1}$$

where U_o and U_w are the superficial velocities, Q_o and Q_w are the volumetric flow rates of oil and water phase, respectively. $A = \pi R_2^2$ denotes the cross sectional area of the pipe. The bulk velocity of each phase is defined as:

$$\bar{U}_o = Q_o/A_o, \bar{U}_w = Q_o/A_o, \tag{2-2}$$

where $A_o = \pi R_1^2$ and $A_w = \pi(R_2^2 - R_1^2)$ are the cross sectional areas of the oil core and of the water annulus, respectively. Note that this definition assumes that there is a perfect core-annular flow (PCAF), where the cylindrical core is located in the centre of the pipe without wavy interface. Similarly, the volume-equivalent radius of the oil core in the flow with the wavy interface can be calculated as $R_1 = \sqrt{V_o/L\pi}$. Here V_o is the volume of the oil and L is the length of the pipe. The ratio of the water volumetric flow rate and the total volumetric flow rate is defined as the watercut:

$$\varepsilon = \frac{Q_w}{Q_w + Q_o}. \tag{2-3}$$

Besides this, the hold-up ratio of the oil and water is defined as:

$$H = \frac{Q_o/Q_w}{V_o/V_w} = \bar{U}_o/\bar{U}_w. \tag{2-4}$$

Bai et al. (1992) found that in the vertical bamboo-wave core-annular flow, $H = 1.39$ is a typical number which is independent of the flow rate. Subsequent research for both vertical and horizontal pipe flow have applied this hold-up ratio in the simulations (Ingen Housz et al., 2017; Beerens et al., 2014; Konings, 2017), and it was also used in the present research.

2-2 Force analysis and dimensionless numbers

The governing forces on the core-annular flow in a horizontal pipe are analyzed from a macroscopic view point. Using the characteristic length scale L and the characteristic velocity scale U, five forces can be distinguished:

- Pressure force $\sim \Delta p L^2$
- Inertia force $\sim \rho U^2 L^2$
- Gravity force $\sim \rho g L^3$
- Viscous force $\sim \mu U L$
- Surface tension force $\sim \sigma L$

Based on the force analysis, several dimensionless numbers are found from the theoretical analysis. The Reynolds number, denoted as the ratio of the inertial force to the viscous force, $Re = LU\rho/\mu$, is widely used for the consideration of efficient oil transport. The driving force of each phase is nondimensionalized as:

$$K = \frac{\partial p/\partial z + \rho_o g}{\partial p/\partial z + \rho_w g}, \tag{2-5}$$

where z is the streamwise direction. In horizontal pipe flow, this number is always equal to 1 because the gravity only works in the radial and circumferential directions.

Considering the fluid parameters, several dimensionless numbers are widely used in the linear stability analysis carried out by Bai et al. (1992). For comparison, these dimensionless are defined as follows:

$$m = \frac{\nu_o}{\nu_w}, a = \frac{R_2}{R_1}, \xi = \frac{\rho_o}{\rho_w}. \tag{2-6}$$

It is quite convenient to use these numbers to specify the flow conditions of the core-annular flow.

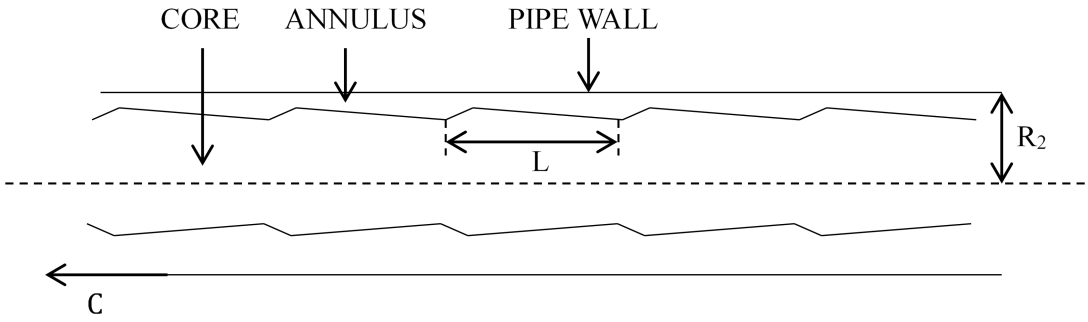

Figure 2-1: Levitation

2-3 Model of levitation

It is found, both in the simulations and in the experiments, that the density difference between the water and oil creates a buoyancy force that pushes the oil-core to the top wall. Despite this, the water annulus at the top is kept at certain conditions. This is a surprising property called the core levitation. Various studies have proven that the waves appearing at the interface play a crucial role in this process. Figure 2-1 shows the lubrication mechanism of the core levitation, where the shape of the interface waves was anticipated at first. In the original theoretic model proposed by Ooms et al. (1984), the core is assumed to be solid and at rest with the wall moving at constant velocity C. A theoretical analysis has shown that the ripples on the interface which are moving with respect to the pipe wall, can generate pressure variations in the annular layer, exerting a counterbalance force to the buoyancy force. Following the semi-empirical model, Ooms et al. (2013) validated the levitation model both at high and low Reynolds numbers with the help of numerical simulation. It was found that the required pressure in the force balance for the levitation can only be reached when the Reynolds number is higher than a threshold number. On the other hand, in the low-Reynolds-number region, the levitation is caused by the lubrication (viscous) force exerted on the narrow gap between the core and the top wall. Using the theory by Ooms et al., the levitation model of horizontal pipe flow will be checked in Chapter 5.

2-4 Experiments set up for comparison

The experimental studies of the core-annular flow in a horizontal pipe have been carried out at 23.4, 30.3, 39.1, 47.6 °C by Duin (2016) previously. Figure 2-2 shows the typical flow pattern of core-annular flow in front view at 23.4 °C(which gives an oil viscosity of 2510 cSt). The flow was measured in a horizontal pipe with the inner diameter of 10.5 mm and the length of 1 metre. For simplicity, the corresponding numerical simulations were implemented at 20, 30, 40, 50 °C in the 2D and 3D domains with the same diameter while much shorter pipe length. The water and oil properties are given in table 2-1 at the different temperatures for the numerical simulations.

Table 2-1: Oil and water properties for simulations at 20, 30, 40 and $50\,^{\circ}\mathrm{C}$

Temperature [°C]	ν_o [cSt]	ν_w [cSt]	ρ_o [kg/m^3]	ρ_w [kg/m^3]
20	3338	1.00	912	998
30	1472	0.80	906	996
40	718	0.66	902	993
50	383	0.55	896	989

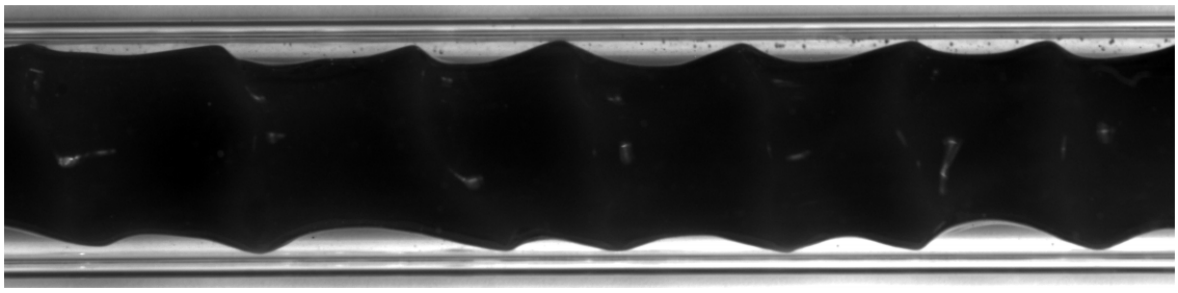

Figure 2-2: Typical core-annular pattern for $Q_o = 0.35$ l/s, $\varepsilon = 20\%$ and $\nu_o \approx 2510$ cSt

Chapter 3

Numerical implementation

The mathematical models of the core-annular flow and the numerical algorithm of the simulations are discussed in this chapter. Based on the Volume of Fluid (VOF) method, we will introduce the governing equations of the two-fluid system. Next, the two alternative interface capturing methods, CVOF and CLSVOF, will be compared and discussed in addition to the common version of VOF. After that, the Launder-Sharma k-ϵ turbulence model will be briefly introduced, accompanied with the parameter definition. Finally, the numerical algorithm of the simulation will be explained in detail based on the systematic introduction of OpenFOAM, the CLSVOF method, and the parallel calculation.

3-1 Volume of Fluid method

The Volume of Fluid (VOF) method has been widely applied to porous-media flows, fluidized beds, bubble columns, and slurry transport in pipelines, to name a few applications. The basic idea of the method is to model the two separate phases as a continuum in space such that only the large-scale flow field is computed explicitly. Accordingly, the small scale heterogeneities are filtered out within the averaging volume. Thanks to the simplification, a coarse grid can be applied for a relatively accurate numerical simulation, which makes the computational expense relatively small. Therefore this provides the feasibility to solve industrial-scale problems. Theoretically, the flow is spatially decomposed into two parts

$$u_\alpha = \langle u_\alpha \rangle^\alpha + \tilde{u}_\alpha, \tag{3-1}$$

where $\langle u_\alpha \rangle^\alpha$ denotes the velocity of the macroscopic flow and $\tilde{u}_\alpha$ denotes the microscopic or subfilter-scale flow. It is assumed that the filter length scale l_a satisfies

$$l_{micro} \ll l_a \ll l_{macro}, \tag{3-2}$$

i.e., this is in between the typical length scale of the microscopic and macroscopic processes, meaning the macroscopic flow is approximately constant over the spatial extent of the averaging volume. The detailed derivation of this method can be found in Brennen (2005). Using

the VOF method, several properties of the mixture flow can be defined,

$$\rho_m = \alpha\rho_o + (1-\alpha)\rho_w \tag{3-3}$$

$$\nu_m = \alpha\nu_o + (1-\alpha)\nu_w, \tag{3-4}$$

here α denotes the scalar indicator of the volume fraction, which is between zero and one. The subscript o denotes the oil phase, which is found in the core, and the subscript w denotes the water phase, which is found in the annulus.

3-2 Governing equations

When we consider the unsteady periodic core-annular flow with two co-current immiscible, incompressible fluids in a horizontal pipe, the governing equations in Cartesian coordinates can be formulated as

$$\frac{\partial\alpha}{\partial t} + \frac{\partial u_i\alpha}{\partial x_i} = 0 \tag{3-5}$$

$$\frac{\partial\rho u_i}{\partial x_i} = 0 \tag{3-6}$$

$$\frac{\partial u_i}{\partial t} + u_j\frac{\partial u_i}{\partial x_j} = -\frac{1}{\rho}\frac{\partial p}{\partial x_i} + \nu\frac{\partial^2 u_i}{\partial x_j^2} + g_i + \frac{1}{\rho}s_i^*, \tag{3-7}$$

where the subscript i denotes the x, y, z direction, $s_i^* = -\sigma^*\kappa\frac{\partial\alpha}{\partial x_i}$ represents the surface tension term from the continuum surface force (CSF) model (Brackbill et al., 1992), the κ denotes the local interfacial curvature. Through the CSF model, the surface tension effect at the interface is formulated as a smooth function defined around the interface with a finite thickness. Equation 3-5 describes the advection of the volume fraction. The material properties of the mixture liquid are described by equations 3-3 and 3-4. The core is asymmetric due to the gravity force and the density difference, which means that the velocity variation in circumferential direction will be taken into account.

3-3 Interface capturing method

As the volume fraction is used for the indicator function in the separated flow system, the two phases are distinguished by the sharp interface, with $\alpha_o = 1$ on one side (oil phase), and $\alpha_o = 0$ on the other side (water phase). The interface captured by the standard VOF method is accomplished by a sub-scale level reconstruction with the line across the $\alpha_o = 0.5$ position using linear or quadratic polynomials (Renardy and Renardy, 2002). Consequently, the normal vector on the interface and the curvature of the interface can be calculated implicitly. This method has been proven to conserve the mass while the interface may experience a severe discontinuity and excessive diffusion, which are caused by the discontinuous nature of the volume fraction, as shown in figure 3-1.

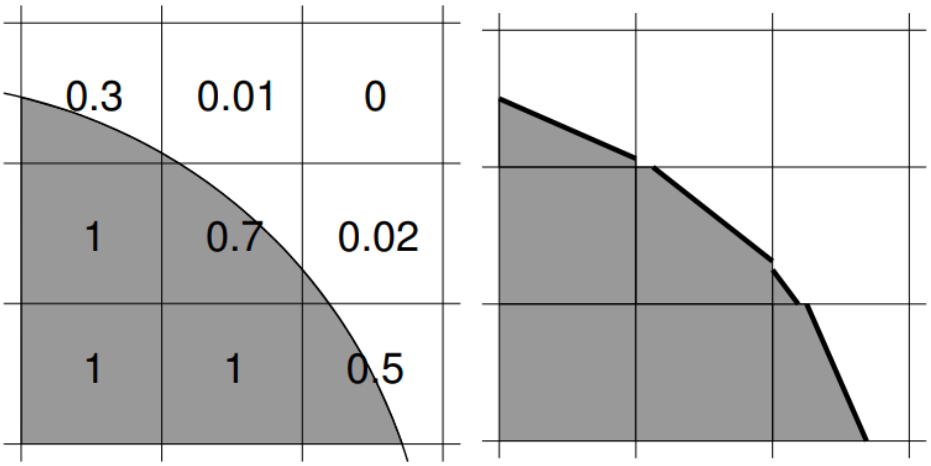

(a) Analytic interface reconstructed from the volume fraction

(b) Piecewise linear interface reconstruction

Figure 3-1: Interface reconstructed using an analytic approach with a piecewise linear approximation; the discontinuity occurs at the reconstructed line

3-3-1 Compressive Volume of Fluid method

An alternative approach to avoid the previously mentioned problem of excessive diffusion is to modify the advection equation of the indicator function itself. Since version 2.1.1, OpenFOAM has included a methodology based on a compressive interfacial treatment of the indicator advection in the two-phase solver **interFOAM**; here we call this the Compressive Volume of Fluid (CVOF) method. The methodology is described below.

By introducing an additional artificial compression term, the advection of the volume fraction in equation 3-5 can be rewritten as:

$$\frac{\partial \alpha}{\partial t} + \nabla \cdot (U\alpha) + \nabla \cdot (U_r \alpha(1-\alpha)) = 0, \tag{3-8}$$

where U_r is an appropriately chosen velocity to compress the interface. The selection of the velocity is done as follows:

$$U_r = \min(c_\alpha |U|, \max(|U|)), \tag{3-9}$$

here c_α is a constant. Setting its value equals to 1.5 gives good results, as suggested by Henrik Rusche (2002). Accordingly, the discretized compressive advection function is formulated as:

$$[\![\frac{\partial [\alpha]}{\partial t}]\!] = -\frac{1}{|\Omega_j|} \sum_{f \in \partial\Omega_j} F_f, \quad F_f = \phi_f \alpha + \lambda_M \phi_{rf} \alpha(1-\alpha), \tag{3-10}$$

where Ω_j denotes the computational cell, F_f denotes the advective flux at the cell face, and $\phi_f = U_f \cdot S$ is the volumetric face flux, in which S is the surface area vector. For simplicity here α represents the volume fraction of oil. Since the cell-centered storage mode is applied in OpenFOAM, the velocity term at the face can be interpolated with various schemes. The specific choices for the numerical parameters for the different simulations are given in Chapters 4 and 5.

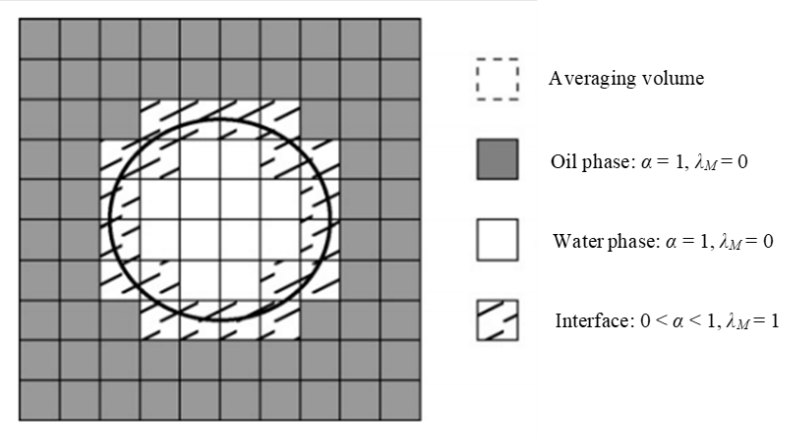

Figure 3-2: Schematic of the MULES delimiter λ_M.

The key feature of this method is to introduce a limiter λ_M to the advection fluxes, which is the Multidimensional Universal Limiter with Explicit Solution (MULES) solver for a bounded solution. The limiter λ_M is equal to one in the interface region and zero elsewhere, as is illustrated in figure 3-2. Therefore, the compressive scheme is only activated within the interface region. The detailed derivation is given in Deshpande et al. (2012). The artificial higher order scheme can not only alleviate the numerical diffusion at the interface, but it also reduces the computational effort. However, further simulations will show that the numerical diffusion away from the interface is still present with this treatment, leading to the dispersion of oil droplets into the water layer.

3-3-2 Coupled Level Set and Volume of Fluid method

Instead of the algebraic treatment in the advection equation, there is another geometric approach for the interface capturing, which is the level set function, written as Φ. Defined as the function for the normal distance to the interface, Φ is zero at the interface and the sign of it can differ around the interface. It gives explicit expressions for the interfacial curvature and for the normal vector without the need to used an additional interface reconstruction approximation. The local mean curvature can be written as:

$$\kappa(\Phi) = \nabla \cdot \frac{\nabla \Phi}{|\nabla \Phi|}. \tag{3-11}$$

Additionally, a new indicator function, which is the Heaviside function H, is defined to distinguish the two phases:

$$H(\Phi) = \begin{cases} 1, & \Phi > 0 \\ 0, & \text{otherwise.} \end{cases} \tag{3-12}$$

Strictly the value of the indicator function is limited to the range between 0 and 1. It is more accurate to distinguish between the two phases through this function than by using the volume fraction. Accordingly, the mixture density and viscosity of the fluid can now be

written as:

$$\rho = \rho_o H(\Phi) + \rho_w(1 - H(\Phi)) \tag{3-13}$$

$$\mu = \mu_o H(\Phi) + \mu_w(1 - H(\Phi)). \tag{3-14}$$

Although the jump in the properties that arises from the Heaviside function is close to the physical conditions, it is difficult to be handled by the numerical simulation, especially at the oil/water interface where the oil-to-water viscosity ratio can be large. Consequently, a regularized Heaviside function is more often used as the indicator function:

$$H_\epsilon(\Phi) = \begin{cases} 0, & \Phi < -\chi \\ \frac{1}{2}[1 + \frac{\Phi}{\chi} + \frac{1}{\pi}\sin \pi\Phi/\chi], & |\Phi| \leq \chi \\ 1, & \Phi > \chi, \end{cases} \tag{3-15}$$

here χ is half of the thickness of the interface region, as pre-defined by the users. It is suggested to chose $\chi = \frac{3}{2}h$, and h is the typical height of the cell at the interface. In this way the interface has a thickness of approximately $\frac{2\chi}{|\nabla\Phi|}$. Note that $\nabla\Phi = 1$ in the transition region is the premise of a uniform thickness χ.

Similar as for the volume fraction, the advection equation for the level set function can also be included in the governing equations:

$$\frac{\partial \Phi}{\partial t} + \nabla \cdot (U\Phi) = 0. \tag{3-16}$$

Based on the curvature and on the Heaviside function, the surface tension force in equation 3-7 can be written as a function of Φ:

$$s_i^* = -\sigma^* \kappa(\Phi) \nabla H(\Phi). \tag{3-17}$$

Using the chain law, the gradient of the Heaviside function can be written as $\nabla H(\Phi) = \delta_\chi(\Phi)\nabla(\Phi)$, where $\delta_\chi(\Phi)$ is the derived from equation 3-15:

$$\delta_\chi(\Phi) = \frac{dH_\chi}{d\Phi} = \begin{cases} 0, & |\Phi| > \chi \\ \frac{1}{2\chi}(1 + \cos\frac{\pi\Phi}{\chi}), & |\Phi| \leq \chi. \end{cases} \tag{3-18}$$

During the simulation, between every two subsequent time steps, a re-distancing method (Sussman et al., 1994) is necessary to keep Φ the normal distance to the interface. This is accomplished by solving the following equation:

$$\begin{aligned} \frac{\partial}{\partial \tau}\Phi &= \text{sgn}(\phi_0)(1 - |\nabla\Phi|) \\ \Phi(x, 0) &= \Phi_0(x), \end{aligned} \tag{3-19}$$

where τ is the artificial time step, chosen as $\tau = 0.1\Delta x$, and sgn is the sign function. Φ_0 is the zero level in Φ, namely the oil-water interface in our case. The solution is converged when $|\nabla\Phi| = 1$ is reached.

Despite the capability of handling topological changes at fluid interfaces, as suggested by Chang et al. (1996), the level set function is not able to guarantee mass conservation. A significant improvement of the VOF function and of the LS function has been proposed by

Sussman and Puckett (2000), which is the Coupled Level Set and Volume of Fluid (CLSVOF) method. This method is organized in a way that both mass is preserved and numerical diffusion at the interface is decreased. The coupling process is accomplished by re-initializing the level set function using the corresponding volume fraction function as obtained by the solver at the same time instant.

The methodology is based on the compressive scheme of the VOF method in OpenFOAM. That is to say, the advection of the volume fraction is calculated as the indicator function during the simulation. The additional level set function contributes to the reconstruction of the interfacial information, especially the interface curvature. The latter plays a crucial role in the momentum equations through equation 3-17. In every time step, after the iteration of the volume fraction with the advection function, the density and viscosity in every computational cell can be updated with equation 3-3 and 3-4, as well as with the zero level set (interface) of Φ through:

$$\Phi_0 = (2\alpha - 1)\chi. \tag{3-20}$$

Here the iso-contour of $\alpha = 0.5$ is used. Hereafter, the re-initializing procedure is applied through solving equation 3-19. The influence of the level set function on the volume fraction is implicitly imposed through the smoothed surface tension term, which is strictly equal to zero outside the interface region as defined by χ and the zero level set. After the re-initialization process, the velocity equations and momentum predictor equations are solved to complete a full iteration loop in a single time step. The numerical algorithm of the CLSVOF method is shown in figure 3-3.

3-4 Turbulence model

In this section, first the RANS equations will be introduced. Following this, the Launder-Sharma low-Reynolds-number $k - \epsilon$ turbulence model and the parameters of it will be presented. Turbulence is widely found in the transport of core-annular flow, especially in the annulus due to the low viscosity of water. Although several numerical studies have been conducted with DNS by Kim and Choi (2018); Li and Renardy (1999); Bai et al. (1996), the computational expense to fully resolve the flow properties in the turbulence region is very high. Generally, using the Reynolds-averaged Navier-Stokes (RANS) equations allows one to solve the flow properties statistically. The averaging process is adopted to properties like the velocity field and the pressure field, in which the quantities are decomposed into an ensemble average term and a fluctuation term:

$$\begin{aligned} u_i &= \overline{u_i} + u_i' \\ p &= \overline{p} + p' \end{aligned} \tag{3-21}$$

Then these terms are substituted into the continuity equation and into the Navier-Stokes equations with the Boussinesq approximation. Note that with this approximation, the density difference due to VOF method will only occur in the gravity term. Thereafter, the time-averaging procedure is applied to the equations to obtain the RANS equations.

Within the equations, there are new averaging terms of the velocity fluctuations, $\overline{u_i' u_j'}$, which can be referred to as the Reynolds stress. These terms, as widely used in turbulence modelling,

are similar to the molecular stress:

$$\rho(-\overline{u_i' u_j'}) = \rho\nu_t(\frac{\partial u_i}{\partial x_j} + \frac{\partial u_j}{\partial x_i}) \sim \rho\nu(\frac{\partial u_i}{\partial x_j} + \frac{\partial u_j}{\partial x_i}), \tag{3-22}$$

where ν_t is the so-called 'eddy viscosity' or 'turbulence viscosity'. It is no longer a material property of the fluid, but instead it depends on the intensity of the turbulence. An appropriate turbulence model for the eddy viscosity is required for the closure of the terms.

3-4-1 Launder-Sharma $k-\epsilon$ model

Recently, in some previous projects on core-annular flow at our university, much effort has been devoted to obtain the appropriate turbulence model for the core-annular flow in horizontal and vertical pipes. The Launder-Sharma $k-\epsilon$ turbulence mode was the one employed by Ingen Housz et al. (2017); Beerens et al. (2014); Konings (2017) during their Master thesis research projects, and that turbulence model was found to be a reliable model for the prediction of the pressure drop. Before introducing the formulation of the model, two turbulent parameters are defined here:

$$\begin{aligned} \text{Turbulent kinetic energy} : k &= \frac{1}{2}\overline{u_i'^2} \\ \text{Turbulent dissipation rate} : \epsilon &= \nu\overline{\omega_i'^2}, \end{aligned} \tag{3-23}$$

where k is proportional to the diagonal terms of the turbulent stress tensor, and it represents the macro-structure of the turbulence, namely the turbulent kinetic energy. The $\overline{\omega_i'^2}$ term, derived from averaging of the vorticity equation, represents the destruction of turbulence in the micro-structure. Based on the energy cascade, and assuming that the turbulence generation and dissipation reach equilibrium, the turbulence dissipation in the micro-scale,ϵ, is fully determined by the turbulence kinetic energy (TKE), k, supplied in the macro-structure. Through the dimensional analysis, the closure model of the eddy viscosity is then defined as:

$$\nu_t = C_\mu f_\mu \frac{k^2}{\tilde{\epsilon}} \tag{3-24}$$

$$\frac{\partial k}{\partial t} + \frac{\partial k u_i}{\partial x_i} = \nu_t \left(\frac{\partial u_i}{\partial x_i}\right)^2 - \epsilon + \frac{\partial}{\partial x_i}\left[\left(\nu + \frac{\nu_t}{\sigma_k}\right)\frac{\partial k}{\partial x_j}\right] \tag{3-25}$$

$$\frac{\partial \tilde{\epsilon}}{\partial t} + \frac{\partial \tilde{\epsilon} u_i}{\partial x_i} = C_{1\epsilon} f_1 \frac{\tilde{\epsilon}}{k}\nu_t \left(\frac{\partial u_i}{\partial x_j}\right)^2 - C_{2\epsilon} f_2 \frac{\tilde{\epsilon}^2}{k} + \frac{\partial}{\partial x_i}\left[\left(\nu + \frac{\nu_t}{\sigma_\epsilon}\right)\frac{\partial \tilde{\epsilon}}{\partial x_j}\right] + 2\nu\nu_T \left(\frac{\partial u_i}{\partial x_i}\right)^2, \tag{3-26}$$

where ϵ is related to the quantity $\tilde{\epsilon}$ through

$$\epsilon = \epsilon_0 + \tilde{\epsilon}, \tag{3-27}$$

and the quantity ϵ_0 is the value of ϵ at the wall.

The equations consist of several adjustable variables σ_k, σ_ϵ, $C_{1\epsilon}$ and $C_{2\epsilon}$, for which the values are given in the Launder-Sharma model as follows:

$$C_\mu = 0.09, \sigma_k = 1, \sigma_\epsilon = 1.3, C_{\epsilon 1} = 1.44, C_{\epsilon_2} = 1.92. \tag{3-28}$$

Since most of the two-equation models fail to predict a realistic value of C_ν, $C_{1\epsilon}$ and $C_{2\epsilon}$ in flow areas with a low local Reynolds number (such as close to the wall), the viscous damping terms (or the so-called low-Reynolds number corrections) are required to account for this (Wilcox, 1993). They were proposed by Launder (1974) with the damping functions f_μ, f_1 and f_2 that are defined as follows:

$$f_\mu = e^{-\frac{3.4}{(1+Re_T/50)^2}}, f_1 = 1, f_2 = 1 - 0.3e^{-Re_T^2}, Re_T = \frac{k^2}{\tilde{\epsilon}\nu} \tag{3-29}$$

3-5 Implementation using the interFOAM solver in OpenFOAM

The simulation model for the multiphase core-annular flow is implemented by using the open-source code library, OpenFOAM. OpenFOAM provides a tensor approach in the finite volume scheme; this has been proven to be an efficient tool for the research of incompressible multi-phase flow (Weller et al., 1998). Theoretically, the governing partial differential equations of the flow are solved by setting up the tensor system with a rank of up to 2 and by organizing the field operations like the divergence and the laplacian in matrix form. By applying the Rhie-Chow interpolation, the variables are stored in the cell centre with the collocated lay-out to avoid numerical oscillations. Additionally, the parallel calculation is easy to achieve via domain decomposition in favor of saving computer time.

3-5-1 Numerical algorithm of interFOAM and CLSVOF

InterFOAM is the VOF based multiphase flow solver in the OpenFOAM code library. Usually, the governing equations are solved with the mixture properties of the fluid while the transport of the interface is updated by solving equation 3-8 with the default compressive scheme of the VOF function. However, the open nature of the code allows the modification for the alternative CLSVOF interface capturing method based on the original method. Figure 3-3 introduces the numerical algorithm of the CLSVOF method implemented in the PIMPLE loop. Here the PIMPLE loop is the coupled solution algorithm of the Semi-Implicit Method for the Pressure-Linked Equation (SIMPLE) and the Pressure Implicit with Spliting of Operators (PISO) for the pressure-velocity coupling in the transient simulation. The solution structure of PIMPLE mainly consists of three steps: momentum prediction, pressure solution and velocity correction. As for the CLSVOF method, the reconstruction of the volume fraction α from the Level-Set function contributes to the sharpness of the interface. In turn, the reconstruction from α to Φ guarantees the mass conservation during the advection.

In addition, based on interFOAM, there are two alternative solvers for the simulation: the pressure-imposed solver and the flux-imposed solver. Basically, the two solvers anticipate the pressure gradient or the total volumetric flow rate as the a-priori known quantity, respectively. Here the flux-imposed solver is the more straightforward solver for the comparison with the experimental data. However, according to the research by Konings (2017), the pressure-imposed solver shows a significant faster convergence speed compared to the other one, hence that one is chosen for the simulations in our study. Meanwhile, considering the periodic boundary conditions applied in our study, the pressure gradient is imposed by adding a constant body force in the streamwise direction to the momentum equation, which means

that the field matrix of of the inlet and outlet cross section can be equal. For the same reason, the buoyant pressure in the simulation is equal to the actual pressure p.

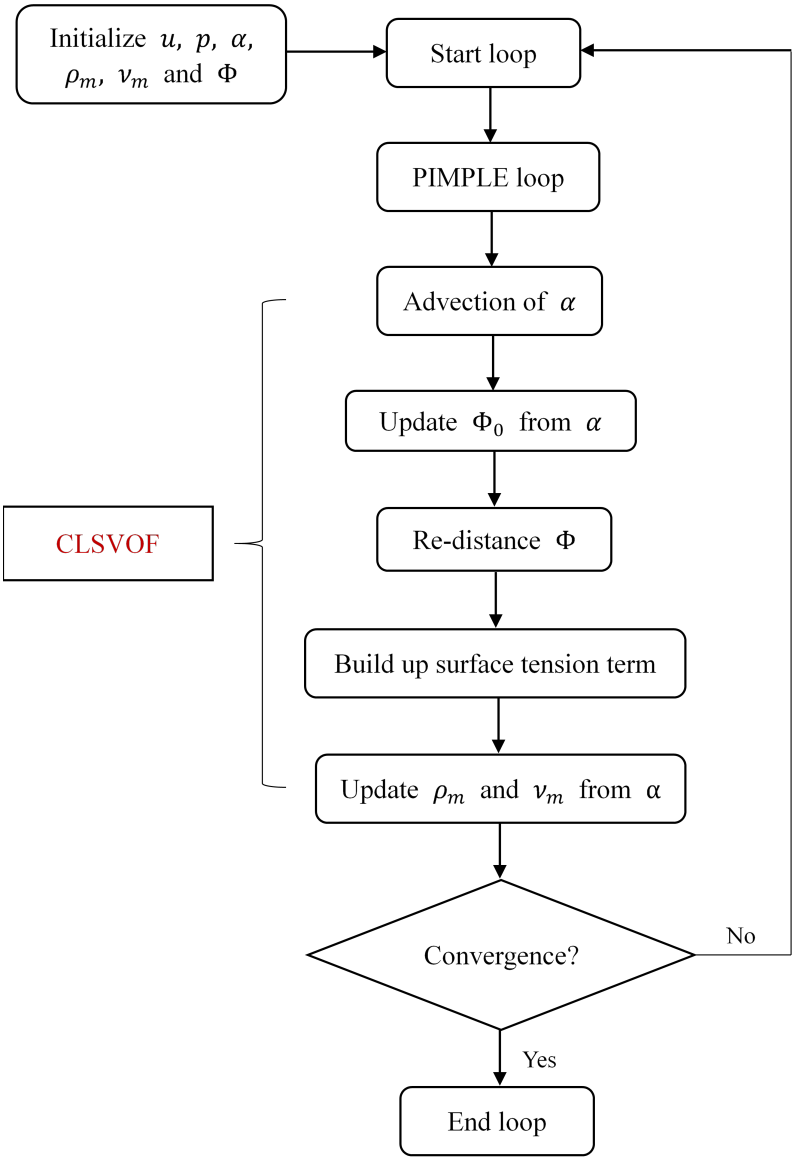

Figure 3-3: Numerical algorithm of the CLSVOF method implemented in the PIMPLE loop

3-5-2 Parallel calculation

A parallel calculation in OpenFOAM can be carried out with domain decomposition. After the initialization, the computational domain is decomposed into several sub-domains following an arbitrary geometry division method in OpenFOAM. For each sub-domain, the simulation loop in a single time step is performed in a pre-assigned core. Between two subsequent time steps, the boundary information is transferred between adjacent sub-domains through

using the standard message passing interface(MPI) library to guarantee the continuity of the solution.

During the calculation, there are mainly two parts in the solution procedure that are time-consuming: the pressure-velocity coupling within each sub-domain and the message communication between the sub-domains. As an example, the 3-D computational domain for a short pipe covered with around a half million grid cells is decomposed in OpenFOAM by using 12 sub-domains (i.e. $2\times2\times3$ in x, y and z direction). It was concluded by Konings (2017) that the efficiency is highest (and the simulation time is lowest) as a function of the applied number of processors numbers when 12 processors are applied to this domain.

Chapter 4

Comparison of the multiphase model with the single-phase model

As mentioned in Chapter 1, the 3D numerical simulation of core-annular flow carried out in the previous research project by Konings (2017) showed a clear deviation for the pressure drop in comparison to the experimental data at a relatively high temperature (i.e. lower oil vicosity). Recommendations were made to investigate the influence of the wavy-interface on the turbulence generation in the annulus. In the following section, we employ the two-phase wedge-shaped model and the single-phase wavy-shaped model, and we will make a comparison of the results. For both models, we focus on the transport characteristics in the lubrication layer by comparing the turbulence distribution and the shear stress induced by the interface and the wall.

4-1 Simulation set up

The simulations with the two models are carried out in OpenFOAM with the Launder-Sharma $k-\epsilon$ turbulence model. The interface capturing method is chosen as the default Volume of Fluid method with the compressive scheme. Using periodic boundary conditions in the main flow direction, a constant pressure gradient is imposed as driving force in the momentum equation in axial direction. The considered pipe has an inner diameter of 21 mm (and its radius is 10.5 mm).

4-1-1 Geometry

As for the multiphase model, which is shown in figure 4-1b, the resolution is 128 $\times$ 128 grid cells with geometrically unequal sizes in radial direction and equal sizes in axial direction. The expansion ratio between the last radial cell at the axis and the first radial cell at the wall is 4. The geometry of the wedge is 25.58 mm $\times$ 10.5 mm in the axial and radial directions. Axisymmetry in the configuration is applied by neglecting the gravity force in the vertical

direction. To resolve the boundary layer fully, the mesh size close to the wall is chosen to satisfy that $y^+ = u_\tau y/\nu_w < 1$, where u_τ is friction velocity calculated as $u_\tau = \sqrt{\tau_w/\rho}$.

The geometry in the single-phase model for the water flow is taken from the shape of the water annulus as obtained in the simulation with the multiphase model at a specific time instant, as shown in 4-1a. The grid has the resolution of 60 × 128 cells, with an unequal grid size in the radial direction and an equal grid size in the axial direction. The height of first grid cell is also controlled to satisfy $y^+ < 1$. In contrast to the multiphase model, the single-phase model is solved in the "water-rest" reference frame, this means the wavy-interface is at rest, but that the pipe wall is moving in the reverse direction to the wave with a speed c. Here c is the axial wave velocity calculated at the corresponding time instant in the multiphase model.

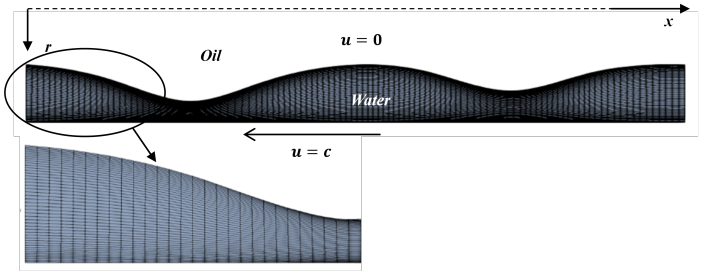

(a) single-phase model

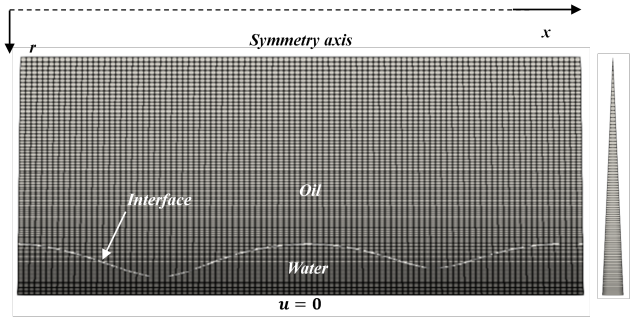

(b) multiphase model

Figure 4-1: Geometry and grid structure of the single-phase and multiphase models at the conditions with H = 1.71, T = 40 °C, P = 1100 Pa/m. The shape of the single-phase model is extracted from the shape of the water annulus in the multiphase simulation at t = 4.78 s.

4-1-2 Discretization and algorithm control

The solver interFOAM is employed for the unsteady multiphase simulation with the default pressure-velocity coupling scheme, PIMPLE. The discretization scheme is based on the Finite Volume Method (FVM), and varies for the different transport terms, as shown in table 4-1. Here the term U_{rb} denotes the artificial velocity field introduced by the compressive scheme of the VOF method, shown in equation 3-9. As for the matrix solver, we select the Preconditioned Conjugate Gradient(PCG) solver with the Diagonal-based Incomplete

Cholesky (DIC) preconditioner for the symmetric positive-definite matrix p_{corr}, where p_{corr} is the pressure correction in the PIMPLE loop. Considering the convergence speed, the Geometric-Algebraic Multi-Grid (GAMG) solver is chosen for the p matrix with the DIC preconditioner. Besides this, as for the other asymmetric matrices like U,ϵ,k, the Preconditioned Bi-Conjugate Gradient (PBiCG) solver is employed with the Diagonal-based Incomplete LU preconditioner(DILU) preconditioner.

Table 4-1: Discretization scheme for the multiphase model

Transport term	**Discretization scheme**
Time scheme	Euler backward
Gradient scheme	Gauss linear
Laplacian scheme	Gauss linear corrected
Interpolation scheme	linear
Divergence scheme	
$\nabla \bullet (\rho U U)$	Gauss limitedLinearV 1
$\nabla \bullet (\epsilon U)$	Gauss upwind
$\nabla \bullet (kU)$	Gauss upwind
$\mu_e \nabla \bullet (\nabla U + \nabla^T U)$	Gauss linear
$\nabla \bullet (\rho \alpha U)$	Gauss vanLeer
$\nabla \bullet (\rho \alpha U_{rb})$	Gauss interfaceCompression

Because the single-phase model is simulated in the steady state, and the multiphase model in transient state, this may influence the relevance of the comparison. Figures 4-2 and 4-3 show the dimensionless interface wave amplitude and the dimensionless water thickness of the multiphase simulation at T = 40 °C over time and in the frequency domain. It is found that the oscillation of the wave amplitude at this condition has a dominant frequency of 12 Hz, which is much less than the reciprocal of the number of time steps per second in the simulation, which is 5×10^4 Hz. Although the shape of the wave varies at different time instants, we accept that we make an approximation by assuming that the wave is fully periodic in the single-phase model.

The steady solver simpleFOAM is employed for the single-phase model with the pressure-velocity coupling scheme, SIMPLE. The discretization scheme is listed in Table 4-2. Note that the density term ρ is left out in the simpleFOAM solver. Similarly, almost all applied matrix solvers are chosen the same as those in the multiphase model, expect for the one to solve for p. For the latter, the PCG solver is selected to improve the convergence accuracy. This can be done in the single-phase model, as the simulation time in the solver remains relatively low.

For the Courant number, the following restriction is used:

$$Co = \Delta t \sum_{i=1}^{3} \frac{u_i}{\Delta x_i} < 0.01, \tag{4-1}$$

where the value 0.01 is the threshold number to get the sharp interface suggested by Rhoheth Radhakrishnan (2016). Meanwhile, since the surface tension plays an important role at the

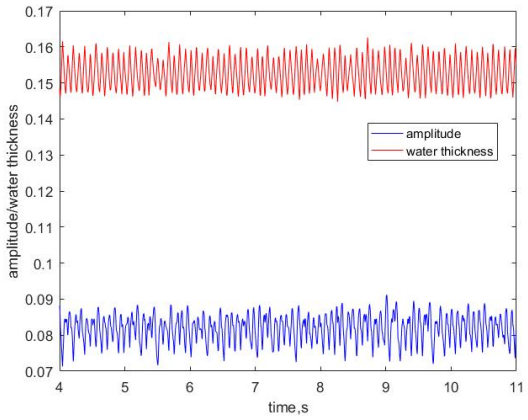

Figure 4-2: Interface wave amplitude at the condition with H = 1.71, T = 40 °C, P = 1100 Pa/m in the time domain

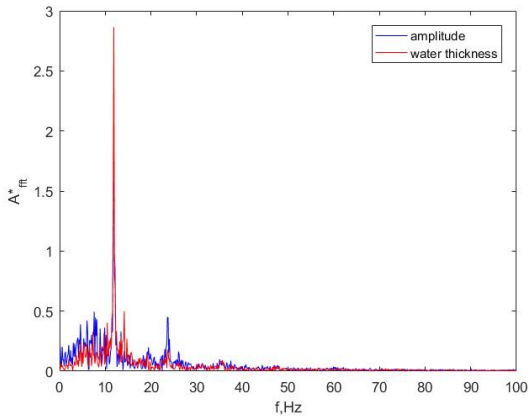

Figure 4-3: Interface wave amplitude at the condition with H = 1.71, T = 40 °C, P = 1100 Pa/m in the frequency domain.

Table 4-2: Discretization scheme for the single-phase model

Transport term	**Discretization scheme**
Time scheme	Euler backward
Gradient scheme	Gauss linear
Laplacian scheme	Gauss linear corrected
Interpolation scheme	linear
Divergence scheme	
$\nabla \bullet (UU)$	Gauss limitedLinearV 1
$\nabla \bullet (\epsilon U)$	Gauss upwind
$\nabla \bullet (kU)$	Gauss upwind
$\nu_e \nabla \bullet (\nabla U + \nabla^T U)$	Gauss linear

interface, the time restriction should also satisfy the following limitation:

$$\Delta t \leq \max(10\tau_\mu, 0.1\tau_p) \quad \text{with} \quad \tau_\mu = \frac{\mu \Delta x}{\sigma} \quad \text{and} \quad \tau_p = \sqrt{\frac{\rho \Delta x^3}{\sigma}}. \tag{4-2}$$

The final values of the Courant number are chosen as $Co = 0.01$, 1 and $\Delta t = 2 \times 10^{-5}$ s, 1×10^{-3} s for multiphase model and for the single-phase model, respectively.

4-1-3 Boundary conditions and initialization

Periodic boundary conditions are used for both models, which are implemented by equalizing the flow values in the cross sections at the inlet and at the outlet. Meanwhile, the Dirichlet boundary condition is applied for U, ϵ and k at the pipe wall, with the constant value of 0 m/s, 1×10^{-15} m^2/s^2 and 1×10^{-15} m^2/s^3, respectively. The Neumann boundary condition is applied for p and α; the spatial derivatives of these two parameters are set to zero.

The flow is initialized with the theoretical results of the PCAF derived by (Li and Renardy, 1999):

$$U(r) = \begin{cases} 1 - \frac{mr^2}{A}, & r \leq R_1 \\ \frac{a^2 - r^2}{A}, & r > R_1 \end{cases} \tag{4-3}$$

$$\alpha(r) = \begin{cases} 1, & r \leq R_1 \\ 0, & r > R_1, \end{cases} \tag{4-4}$$

where the radius of the core is calculated from equation 2-4, which gives:

$$R_1 = \frac{R_2}{\sqrt{(Q_w/Q_o)H + 1}}. \tag{4-5}$$

A sinusoidal type of perturbation is added to the phase interface with an amplitude of 1×10^{-6} m to activate the wave development. The turbulence parameters like k and ϵ are initialized uniformly over the whole pipe with the value of 0.2 m^2/s^2 and 200 m^2/s^3, respectively.

4-2 Comparison for 20 °C (oil viscosity is 3338 cSt)

The flow at the conditions T = 20 °C (oil viscosity is 3338 cSt), H = 1.39, P = 930 Pa/m, m = 3093, is first considered. The hold-up ratio H = 1.39 is taken from Bai et al. (1992), who found that this ratio is independent of the volumetric flow rate; this value was also used in previous studies. From the analysis of the amplitude development we find that the convergence time for the multiphase model is $t_c > 4$ s, and therefore the shape of the wavy interface in the single-phase model is chosen at time t = 4 s. Figure 4-1 compares the geometry of the single-phase model and of the multiphase model at the conditions with T = 40 °C, H = 1.71, P = 1100 Pa/m, m = 1150; the results for this 40 °C case will be discussed in the next section.

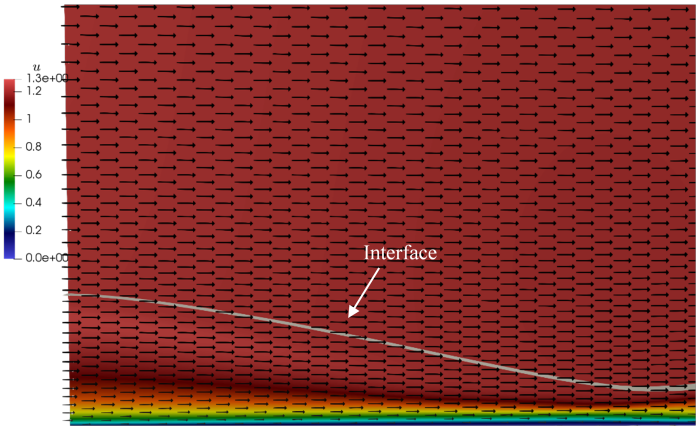

Figure 4-4: Instantaneous velocity vector distribution near the wave crest and near the trough at the conditions with H = 1.39, T = 20 °C , P = 930 Pa/m in the stationary reference frame.

Figure 4-4 shows the instantaneous velocity vector distribution around the wave crest and trough in the multiphase model. The wave number at this condition is 1. The Reynolds number, $Re_a = \bar{h}_a \bar{u}_a / \nu_w$, in the annulus is 1144 for the single-phase model and 1164 in the

multiphase model. Here $\bar{h}_a$ is the averaged height of the water annulus and $\bar{u}_a$ is the averaged velocity in the annulus. According to the linear stability analysis by Kouris (2001), when the viscosity ratio m is larger than $\mathcal{O}(10^3)$, the flow in the annulus is always unstable. It is also shown in figure 4-6 that the effective viscosity in the annulus is much higher than the viscosity of water, which confirms that the flow in the annulus is turbulent. The driving force of the flow in the annulus consists of the imposed pressure gradient and the shear stress exerted by the interface, making the flow of the Poiseuille-Couette type. Considering that the dimensionless pressure gradient, $\Gamma = -(dP/dz)L/(\rho_w u_{core}^2) < 8.7 \times 10^{-3}$, is quite small, the flow is mainly driven by the moving interface on the top which means that it is closer to the Couette type flow (Polderman et al., 1986).

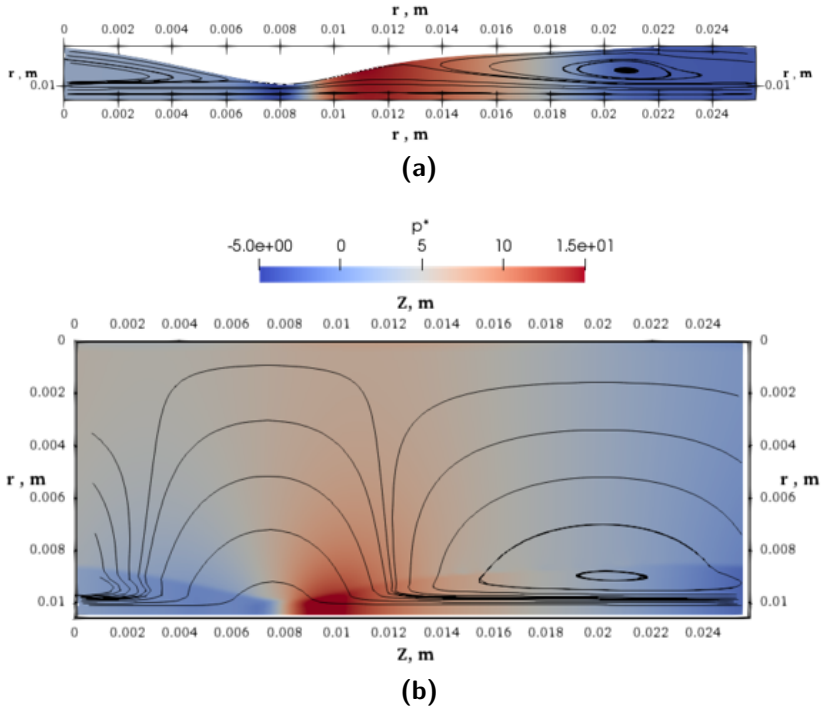

Figure 4-5: Dimensionless pressure distribution and streamlines in the wave-rest reference frame at the conditions with H = 1.39, T = 20 °C , P = 930 Pa/m, t = 4 s:(a) single-phase model,(b) multiphase model. Here $p^* = p/(\rho_w u_\tau^2), u_\tau = \sqrt{\tau/\rho_w}$. The colours denote the pressure, and the black solid lines are streamlines.

Figure 4-5 shows the dimensionless pressure distribution for the two models, combined with the streamlines created in the wave-rest reference frame. The dimensionless pressure is defined as $p^* = p/(\rho_w u_{\tau,b}^2)$ where $u_{\tau,b} = \sqrt{\tau_b/\rho_w}$ is the frictional velocity at the bottom wall. A high stagnation pressure region is found in front of the wave crest accompanied by the adverse pressure gradient around the wave trough. This phenomenon was found by Bai et al. (1996); Ko et al. (2002); Feng et al. (1995) in their numerical simulation for multiphase flow, and it thus is also found in our multiphase model. It seems that the pressure variation over the annulus is larger in the single-phase model compared to that in the multiphase model, which indicates that the energy conversion from static pressure to kinetic energy is more intense in the single-phase model. The adverse pressure gradient at the wave trough causes the flow to separate at the wave crest. Note that the streamlines cut the phase interface in Figure 4-5b.

This is because the velocity vector close to the interface is subtracted from the streamwise wave velocity vector, leading to the change of the direction of the reference velocity, which is now no longer along the curved interface. Theoretically, the leftward shear stress develops from the bottom wall and diffuses in the vertical direction, which is compensated by the rightward pressure gradient. Close to the wave crest, the high pressure force overcomes the shear stress, leading to the flow detachment and further re-circulation. This secondary flow, appearing as recirculation in the wave-rest reference frame, is crucial for the levitation of the core, which will be discussed in Chapter 5. To some extent, the vortex generated by the recirculation enhances the transition from laminar to turbulence flow, leading to the high turbulent kinetic energy and eddy viscosity around the recirculating centre. It was also proven in the 3D simulation at the same condition with $Re_w = 1465$ by Konings (2017) that the hold-up ratio and watercut calculated from the numerical simulation with the turbulence model were quite close to those from the experimental data. Therefore, it is worthwhile to investigate the distribution of the turbulence parameter for the two different models, especially close to the interface.

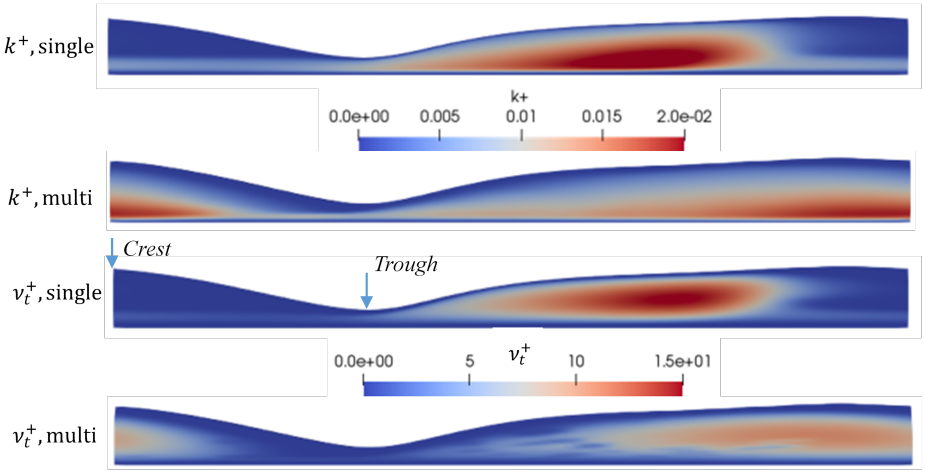

Figure 4-6: Dimensionless turbulent kinetic energy and eddy viscosity in the multiphase and single-phase models at the conditions with T = 20 °C, H = 1.39, P = 930 Pa, m = 3093. Here $k^+ = k/\bar{u_a}^2$ and $\nu_t^+ = \nu_t/\nu_w$, u_a is the velocity in the annulus

Figure 4-6 shows the distribution of the dimensionless turbulent kinetic energy $k^+ = k/(\bar{U_a})^2$ and the eddy viscosity $\nu_t^+ = \nu_t/\nu_w$ in the two models. The highest value of ν_t close to the vortex centre is around 15 times larger than the the kinematic viscosity of water. As mentioned by Nieuwstadt et al. (2016), the turbulence consists of chaotic vortex-like structures with varying dimensions, and therefore this phenomenon can be explained as follows: the Dirichlet boundary condition of the wall-bounded flow at the top wall in the single-phase model is more restrictive for the flow than that of the 'interface-bounded' flow in the annulus of the multiphase model. The conversion process from kinetic energy to pressure energy is more intense with the Diriclet boundary condition, leading to the higher adverse pressure gradient as observed in figure 4-5. Therefore, the flow separation after the wave trough occurs earlier, and is accompanied by the vortex generation. The more intense turbulence level before the wave crest is found in the single-phase model. The focus is on the variation in the vertical direction, which is shown in figure 4-7. The flow field varies between the different models;

see figure 4-6. The turbulence almost disappears at the wave crest in the single-phase model, indicating that the earlier generated vortex is not able to transfer turbulence in downstream direction due to the wall-bounded boundary condition. Between the two models, the velocity field deviates significantly at the wave trough close to the interface/solid wall. We have determined $y^+ = yu_t^*/\nu_w$ at the starting point of the deviation, shown as a circle in the figure, where $u_t^* = \tau_t/\rho_w$ is the frictional velocity on the top wall of the single-phase model. It is calculated that the flow at the location of the deviation has an y^+ equal to 25, which means that this is still in the boundary region of the wall-bounded turbulent flow. Thus the flow in the single-phase model always feels a strong influence from the top and bottom walls while the influence from the top interface on the flow in the multiphase model is less strong. Besides this, among all the flow quantities, the eddy viscosity is one that is most sensitive to the boundary condition, with a more than 5 times decrease in magnitude.

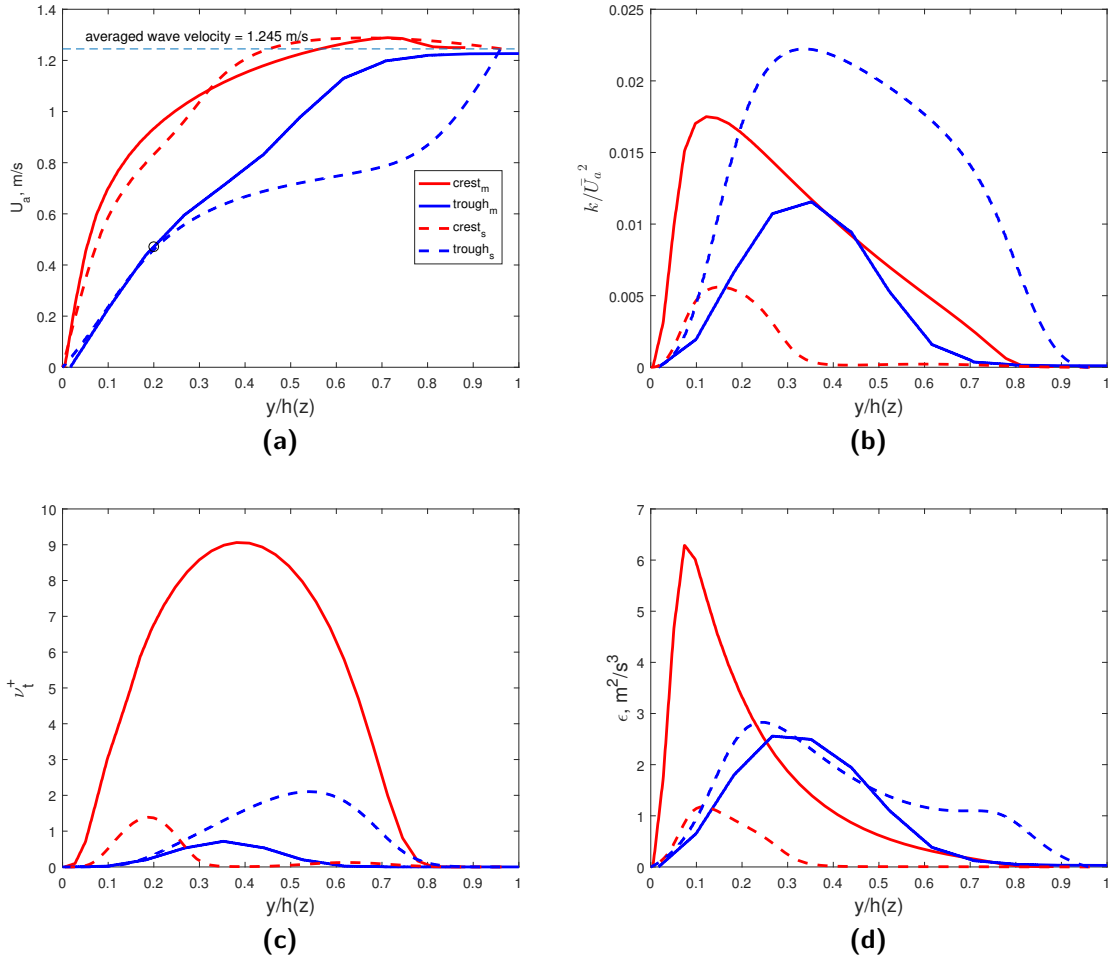

Figure 4-7: Flow field distribution over the cross section at the wave crest and wave trough locations as a function of the y-coordinate in the annulus, where k is nondimensionalized with the averaged velocity of water in the annulus as $k^+ = k/\bar{U_a}^2$, ν_t is nondimensionalized as $\nu_t^+ = \nu_t/\nu_w$, y is nondimensionalized with the height of the annulus $h(z)$, the subscript m denotes the multiphase model, and s denotes the single-phase model

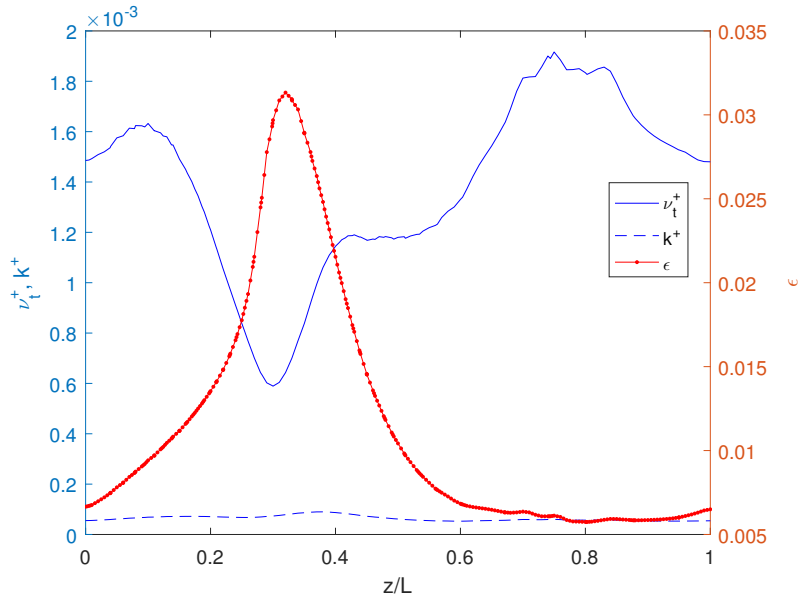

Figure 4-8: Turbulence parameters $k/\bar{U}_a^2$, ϵ, ν_t^+ of the multiphase model at the phase interface along the streamwise direction at t = 4 s, for which the phase interface is defined as $\alpha_o = 0.5$.

The shape of the distribution of the turbulent parameters in the vertical direction is not affected by the boundary condition. Furthermore, the values at the interface decrease to the magnitude of the boundary condition at the wall, as shown in figure 4-8. It is found that the turbulent viscosity at the interface is much smaller than the kinematic viscosity of water, indicating the "solid"-like nature of the oil core.

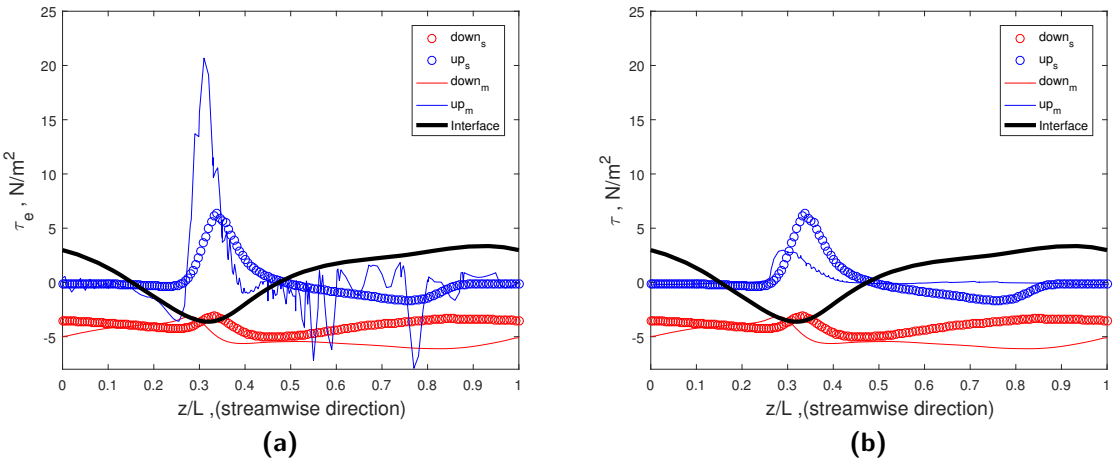

Figure 4-9: Effective shear stress.(a),$\tau_{eff} = (\nu_m + \nu_t)(\nabla U + \nabla^T U)$, where ν_m is the mixture kinematic viscosity using the volume fraction of oil. (b),$\tau_{eff} = (\nu_t + \nu_w)(\nabla U + \nabla^T U)$

We now focus on the shear stress at the interface and at the wall. Figure 4-9 illustrates the effective shear stress $\tau_{eff} = \nu_{eff}(\nabla U + \nabla^T U)$ at the phase interface/top wall and at the

bottom wall. Here $\nu_{eff} = \nu_m + \nu_t$ is the combination of the mixture molecular viscosity and the eddy viscosity. In both models the highest shear stress occurs in the wave trough location while the shear stress at the interface for the multiphase model oscillates very much after the peak. It should be mentioned that the phase interface in the multiphase simulation is a somewhat artificial geometry defined with the assumption that $\alpha = 0.5$. The simulation accuracy is highly dependent on the interface reconstruction and on the diffusion because of the high viscosity ratio, i.e. $m > 3000$. If we assume that a sharp interface is created in the simulation, in which the volume fraction is larger than 0 and smaller than 1, only in a single layer of cells called the interface, then τ_{eff} can be calculated by using the cell just below the interface as $\tau_{eff} = (\nu_t + \nu_w)(\nabla U + \nabla^T U)$, which is illustrated in Figure 4-9(b). The oscillation is smoothened out, accompanied by the decrease of the peak value at the wave trough. Since the eddy viscosity is quite steady and close to zero at the interface, the peak value is caused by the high velocity gradient in the wave trough. However, the significant difference between the two models in Figure 4-9, especially for the oscillation region, is mainly caused by the numerical 'dispersion' of the oil phase as droplets in the water phase in the annulus. This seems to be nonphysical and is due to shortcomings in the VOF method. This dispersion was not found in the experimental investigation by Duin (2016) for the same conditions. This dispersion phenomenon is thus concluded to be a key factor in the prediction of the pressure drop, which will be discussed in Chapter 5.

4-3 Comparison for $40\,^{\circ}\mathrm{C}$ (oil viscosity is 718 cSt)

The flow at the conditions with T = 40 °C (oil viscosity is 718 cSt), H = 1.71, P = 1100 Pa/m, m = 1150 is investigated in this section. The hold-up ratio is taken from the results of the 3D simulation as carried out in the previous research by Konings (2017), where an unexpected large over-prediction of the pressure drop was found. As was also illustrated in Figure 4-1, we extract the shape of annulus after the multiphase simulation reaches convergence, at the time $t = 4.78$ s. That shape is used to create the single-phase model with the same shape. Accordingly, the anticipated moving velocity of the wall in the single-phase model is $c = 1.51$ m/s.

The Reynolds numbers in the water annulus of the single-phase model and of the multiphase model are now 3017 and 3045, which are both larger than the critical value to get turbulent flow in a pipe. Figure 4-10 shows the instantaneous velocity vector field of the multiphase simulation of the 2D wedge-shaped model near the wave crest and near the trough. Roughly, it seems that the height of velocity boundary layer changes gently along the streamwise direction in both models, while the largest thickness at the the wave trough is closer to the top wall in the single-phase model. The difference in the boundary layer can be reached with the displacement thickness $\delta^*(z,t)$ defined as:

$$\int_{R_1}^{R_2-\delta^*} u_{wave} dr = \int_{R_1}^{R_2} u_a dr \tag{4-6}$$

Here $R_1(z,t)$ and R_2 are the radii of the oil core and of the pipe, respectively, and u_a is the velocity in the annulus. The free-stream velocity for both models is chosen as the wave velocity. Note that the equation is only specified for the axisymmetric flow.

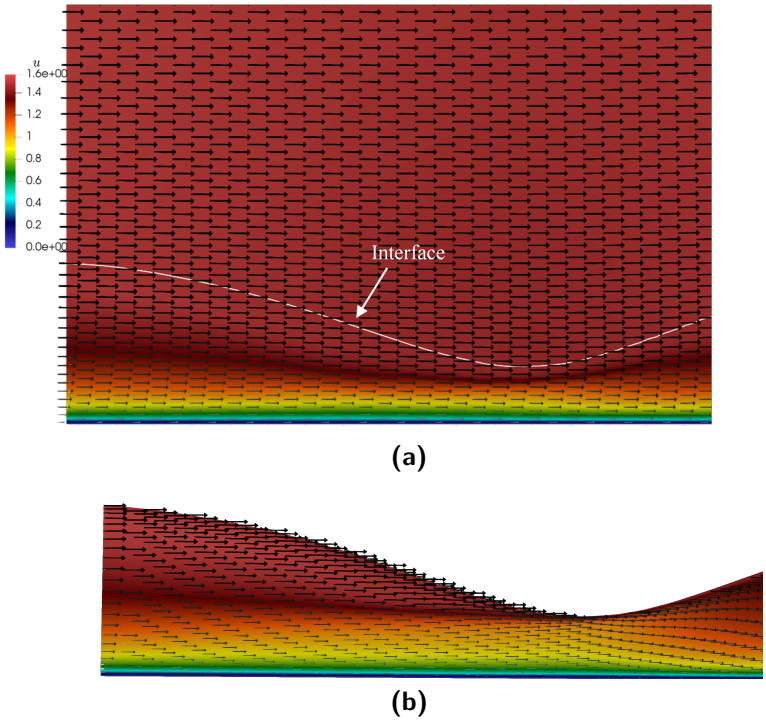

Figure 4-10: Distribution of the instantaneous velocity vector near the wave crest and trough at the conditions with H = 1.71, T = 40 °C, P = 1100 Pa/m in the stationary reference frame.

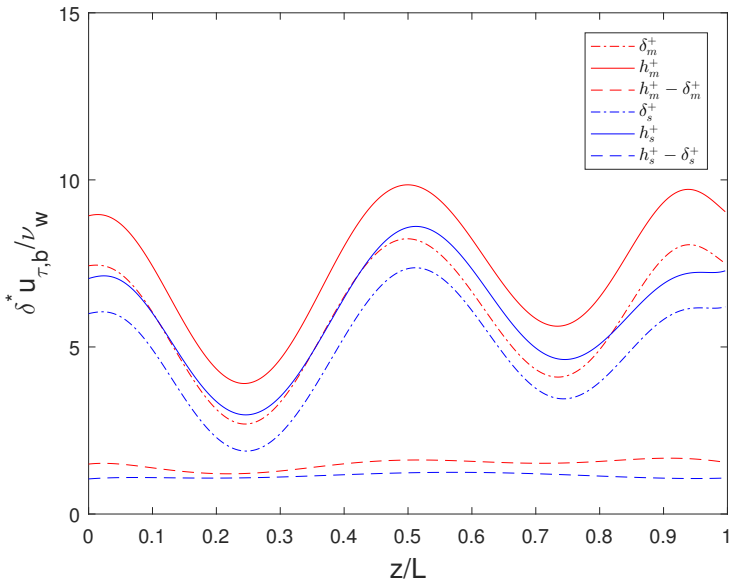

Figure 4-11: Instantaneous streamwise distribution of the dimensionless displacement thickness δ^+(H = 1.71, T = 40 °C, P = 1100 Pa, t = 4.78 s), where $\delta^+ = \delta^* u_\tau/\nu_w$. δ^* is the displacement thickness determined by equation 4-6.

Figure 4-11 shows the dimensionless instantaneous streamwise distribution of the displacement

thickness and of the annulus height, defined with the radial distance from the bottom wall to the top wall/interface. These quantities are nondimensionalized by the local friction velocity $u_{\tau,b}$ and by the kinematic viscosity of water ν_w, where $u_{\tau,b}$ is based on the wall shear stress on the bottom wall. The averaged dimensionless displacement thicknesses are $\bar{\delta}^{*+} = 4.9$ and 6, and the average of dimensionless phase annulus heights are $h^+ = 6$ and 7.3, for the single-phase model and for the multiphase model, respectively. On average, between the two models, the difference in the dimensionless number is around 22%, which reflects the difference of the wall shear stress at the bottom. This is caused by difference in the velocity gradient at the wave trough, as is illustrated in figure 4-14a. Just like in the case with 20 °C, the flow in the small gap at the wave trough is strongly affected by the shear stress from the top wall in the single-phase model, weakening the contribution from the bottom wall. In addition, the displacement thickness is quite close to the annulus height in both models, showing that most of the water still flows within the turbulent boundary layer in the annulus. However, this phenomenon is different from the 3D DNS results by Kim and Choi (2018), who found that the magnitude of the displacement thickness was much smaller than that of the annulus height and was only close to it near the wave crest. The difference can be caused by the use of the coarser grid in our model, which will be insufficient to fully resolve the small-scale deformation of the interface. Another reason could be that the viscosity ratio m is 17.6 times larger in the configuration simulated by Kim and Choi. Nevertheless, the variation trend of δ^* follows the shape of the phase interface in both cases, indicating the positive correlation between the boundary layer thickness and the annulus height in both models.

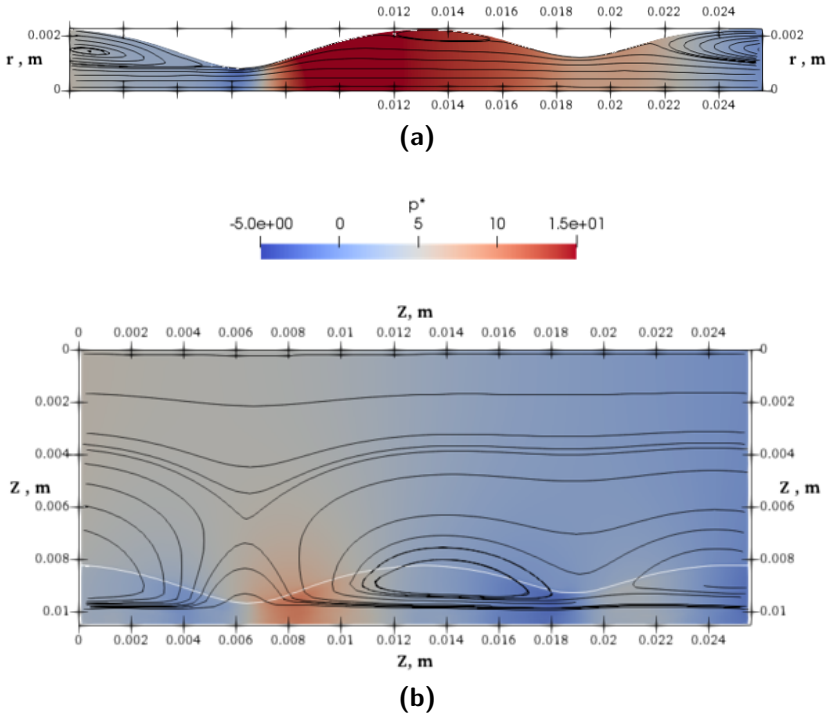

Figure 4-12: Dimensionless pressure distribution and streamlines in the wave-rest reference frame at the condition with h = 1.71, T = 40 °C , dp/dz = 1100 Pa/m:(a) single-phase model,(b) multiphase model. $p^* = p/(\rho_w u_\tau^2), u_\tau = \sqrt{\tau/\rho_w}$.

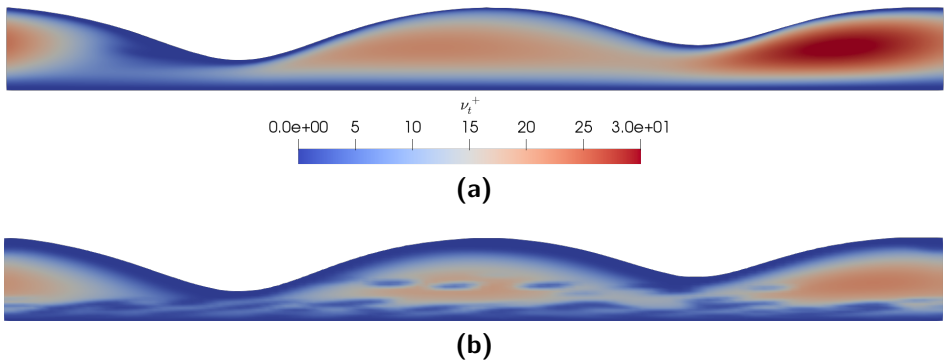

Figure 4-13: Dimensionless eddy viscosity distribution in the annulus at 40 °C, $\nu_t^+ = \nu_t/\nu_w$:(a) single-phase model, (b) multiphase model.

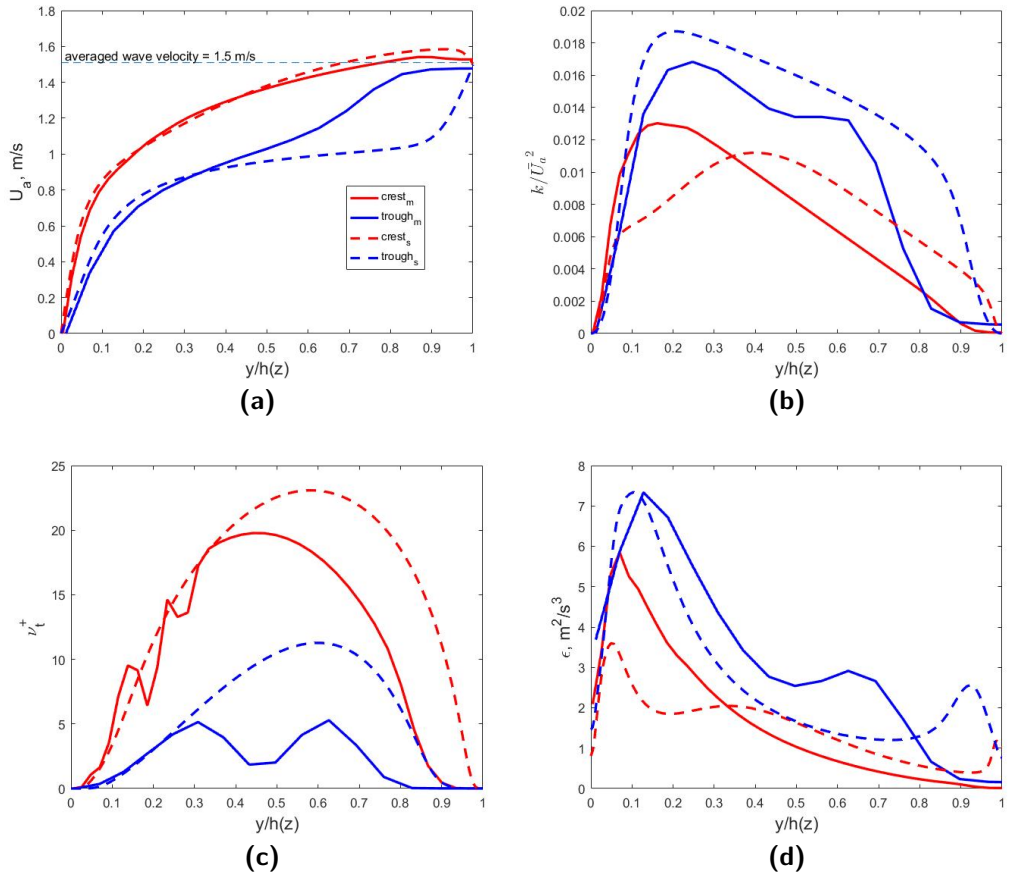

Figure 4-14: Flow field distribution over the cross section at the wave crest and wave trough as a function of the y-coordinate, where k is nondimensionalized by the averaged velocity of the water in the annulus as $k^+ = k/\bar{U_a}^2$, ν_t is nondimensionalized as $\nu_t^+ = \nu_t/\nu_w$, y is nondimensionlzied by the annulus height $h(z)$, the subscript m denotes the multiphase model, s denotes the single-phase model.

At 40 °C the core-annular flow pattern still remains valid with the wave number of 2. In figure

4-12 the recirculation region is also found in front of the wave crest with a weaker adverse pressure in the wave-rest reference frame, compared to that for 20 °C. Since the pressure drop of $dp/dx = 1100$ Pa/m is close to that imposed at the lower temperature, it seems that the increase of the wave number tends to alleviate the pressure variation over the annulus. On the other hand, the oscillating frequency of the water flow rate increases due to the decrease of the wave length, which is consistent with the theoretical derivation from the wave equation $f = u/\lambda$.

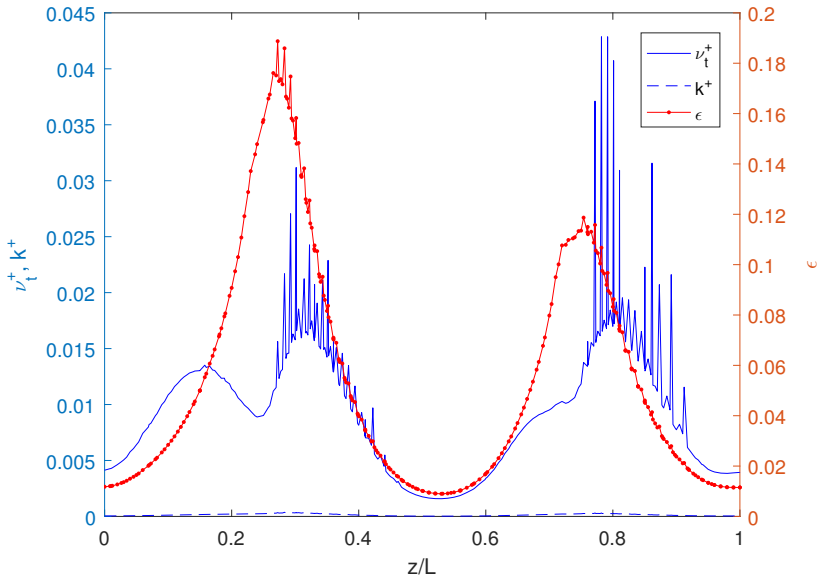

Figure 4-15: Turbulence parameters k^+, ϵ, ν_t^+ for the multiphase model at the phase interface along the streamwise direction at t = 4.78 s, in which the phase interface is defined as $\alpha_o = 0.5$.

Compared to the case with 20 °C, both the turbulent kinetic energy and the turbulence dissipation rate have increased at 40 °C due to the decrease of the molecular viscosity of two phases. Besides this, the region with the concentrated eddy viscosity still appears around the wave crest in the single-phase model, as shown in figure 4-13. On average, the value of ν_t^+, as well as of the turbulent kinetic energy, increase as the viscosity decreases while the distribution shape stays the same as found with higher viscosity. Particularly, in the radial direction, the turbulent kinetic energy and the eddy viscosity are at the same level for the two models now, as shown in figure 4-14. It is found that the top wall and interface still have different influence on the distribution of the turbulence while the difference reduces as viscosity decreases. On the other hand, the throughput of water is quite stable with different boundary condition. If we check the turbulence parameters at the interface for multiphase model, a noticeable oscillation of the eddy viscosity is shown in figure 4-15. Basically, all the turbulence parameters remain at a quite low level; as expected, the interface acts like a solid wall. However, the oscillation is found to be related to the numerical dispersion of the oil phase into the water annulus, as is shown in figure 4-16. Scattered small regions with considerable oil fractions are found close to the bottom wall. The dispersion is also found at the lower temperature, but here it is less evident, since it aggravates with an increase in temperature (i.e.a decrease in oil viscosity). This phenomenon is caused by the compressive scheme of

the Volume of Fluid method applied in interFOAM solver. Details about its influence on the average flow field will be discussed in the next chapter.

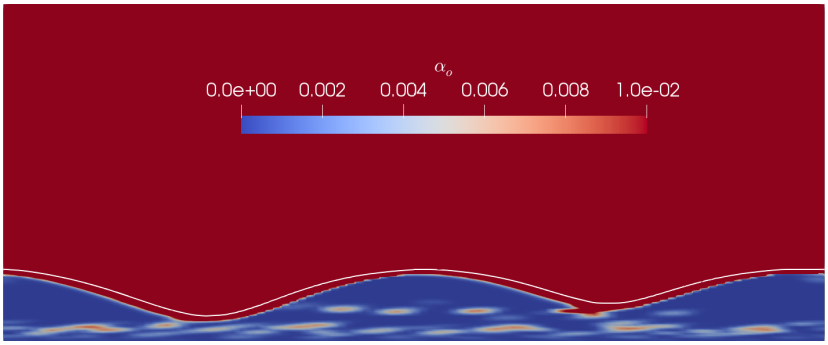

Figure 4-16: Numerical oil dispersion at 40 °C in the 2D wedge-shaped model; the legend for the oil volume fraction is from 0 to 0.01, and the white curve is the phase interface defined as $\alpha_o = 0.5$.

4-4 Conclusion

The turbulent water flow in the annulus has been investigated with the wavy-shaped single-phase model and with the wedge-shaped multiphase model. The steady state wall-bounded single-phase simulation is a valid approximation of the periodic unsteady axisymmetric core-annular flow from the perspective of the water flow rate and the pressure distribution. Several characteristics of the multiphase simulation, like the recirculation around the wave crest in the wave-rest coordinate system, the adverse pressure and the large velocity gradient region at the wave trough, and the dependence of the displacement thickness on the annulus height, etc, can also be found in the single-phase model.

However, the difference between the 'interface-bounded' flow (in the multiphase model) and the 'wall-bounded' flow (in the single-phase model) does exist and plays an important role in the position of the flow separation, the vortex generation and the turbulence generation. Compared to 'interface-bounded' flow, the turbulence is more concentrated in the 'wall-bounded' flow, due to the numerical dispersion of oil into the water annulus. The interface region defined as $0 < \alpha < 1$ is found to have evident thickness around the $\alpha = 0.5$ iso-contour. The thickness is large enough to influence the behavior of 'interface-bounded' flow in the annulus. It is reflected in the shear stress at the phase interface which has an irregular oscillation in the streamwise direction. Meanwhile, since the numerical oil dispersion aggravates with the temperature in the multiphase model, the eddy viscosity at the interface starts to oscillate in the case with 40 °C. The water flow rate is not sensitive to the oil dispersion. This is due to the high dependency on the wave velocity (shear stress) in the Couette-type flow. Thus the prediction of the water flow rate for the two models is always consistent.

Chapter 5

Comparison of the CLSVOF and CVOF methods

The oil/water interface in the core-annular flow has been proven to give some similar characteristics as using a solid wavy wall in the prediction of the throughput for a given pressure drop. However, when it comes to the turbulence distribution, differences are found which are due to the temperature-dependent numerical dispersion of oil in the water annulus. An appropriate interface reconstruction method is required to simulate the jump in the fluid properties across the interface. For that reason, the comparison of the CLSVOF and CVOF methods is based on the 3D simulations. Furthermore, a convergence study with the CLSVOF method is performed based on the 2D wedge-shaped model for a vertical pipe.

Several parameters are defined to quantify the influence of the interface capturing method. The eccentricity of the core is defined as:

$$e = \frac{1/2(y_{crest,top} + y_{trough,top}) - R_1}{R_2 - R_1}, \tag{5-1}$$

and the wave amplitude close to the top wall is:

$$A_{top} = \frac{y_{crest,top} - y_{trough,top}}{2R_1}. \tag{5-2}$$

In order to verify the mass conservation in the simulations, the error in the volume fraction error is evaluated as:

$$\gamma = \frac{|\sum \alpha^I - \sum \alpha^F|}{\sum \alpha^I}, \tag{5-3}$$

here the superscript I denotes the initial condition and F denotes the final condition.

In addition to this, as introduced in the "flying-core" model, the levitation of the core will finally be maintained with a certain eccentricity due to the force balance in the vertical direction. The momentum of the oil-core in the vertical direction will approach zero once the force balance between the pressure force and the buoyancy force has been reached. Therefore,

this is also checked during the simulation as a criterion for the convergence. The integral of the upward momentum of the core is calculated as:

$$M_{o,y} = \rho_o \sum_{j=1}^{N} \alpha_o u_y V_{core}, \tag{5-4}$$

here N denotes the number of cells in the core, u_y is the vertical velocity and V_{core} represents the volume of each cell in the core.

5-1 3D simulation with the CVOF method

In the previous research by Konings (2017), a systematic investigation on the pressure drop prediction of the horizontal core-annular flow was carried out with the 3D simulations at different working conditions. Those simulations were done with the Launder-Sharma low-Re $k-\epsilon$ turbulence model and with the interFOAM solver in OpenFOAM. Using the default interface capturing method, CVOF, the simulation results showed a good agreement with the experimental data obtained by Duin (2016) at 20 °C. However, applying the linear interpolation at 40 °C, the simulation data largely over-predicted the pressure gradient at the condition with a high water-cut, as is illustrated in figure 5-1.

A simulation with the flux-imposed solver (Konings, 2017) is then conducted with the same Q_a and H as in the experiments with the 1122 Pa/m pressure gradient. It was found that the over-prediction of the pressure drop is 152%, considering the predicted value of 2830 Pa/m. In fact, the predicted pressure gradient deviates more from the experimental data when the water-cut increases.

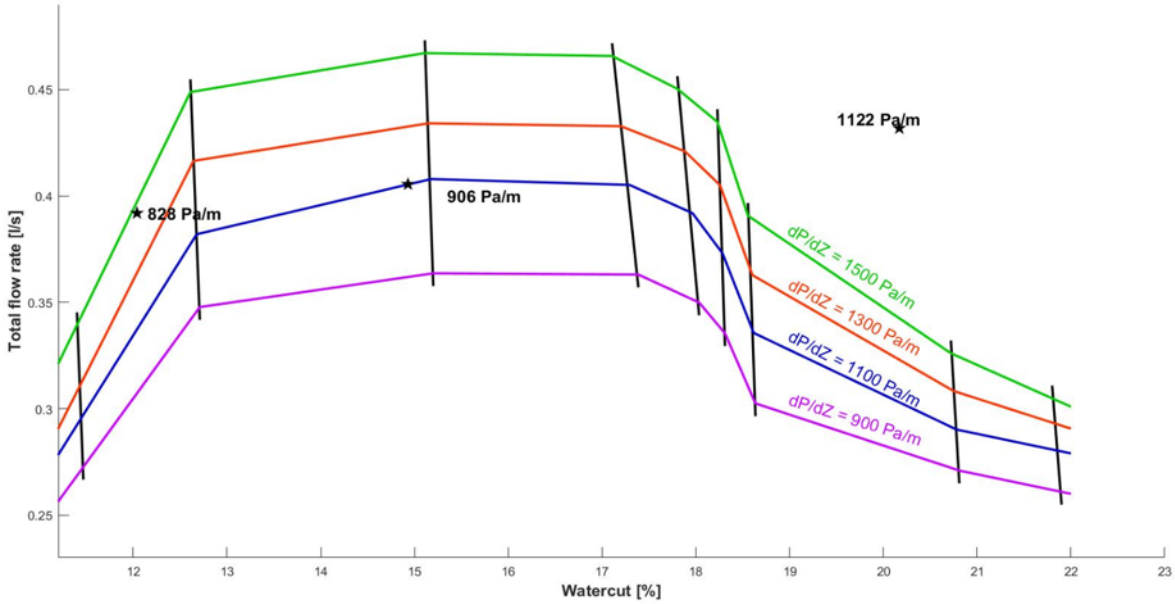

Figure 5-1: The water-cut and total flow rate for different holdup fractions (black lines) and the pressure gradients (colored lines) as predicted with the VOF method at 40 °C. Black star: experimental datas; figure taken from Konings (2017)

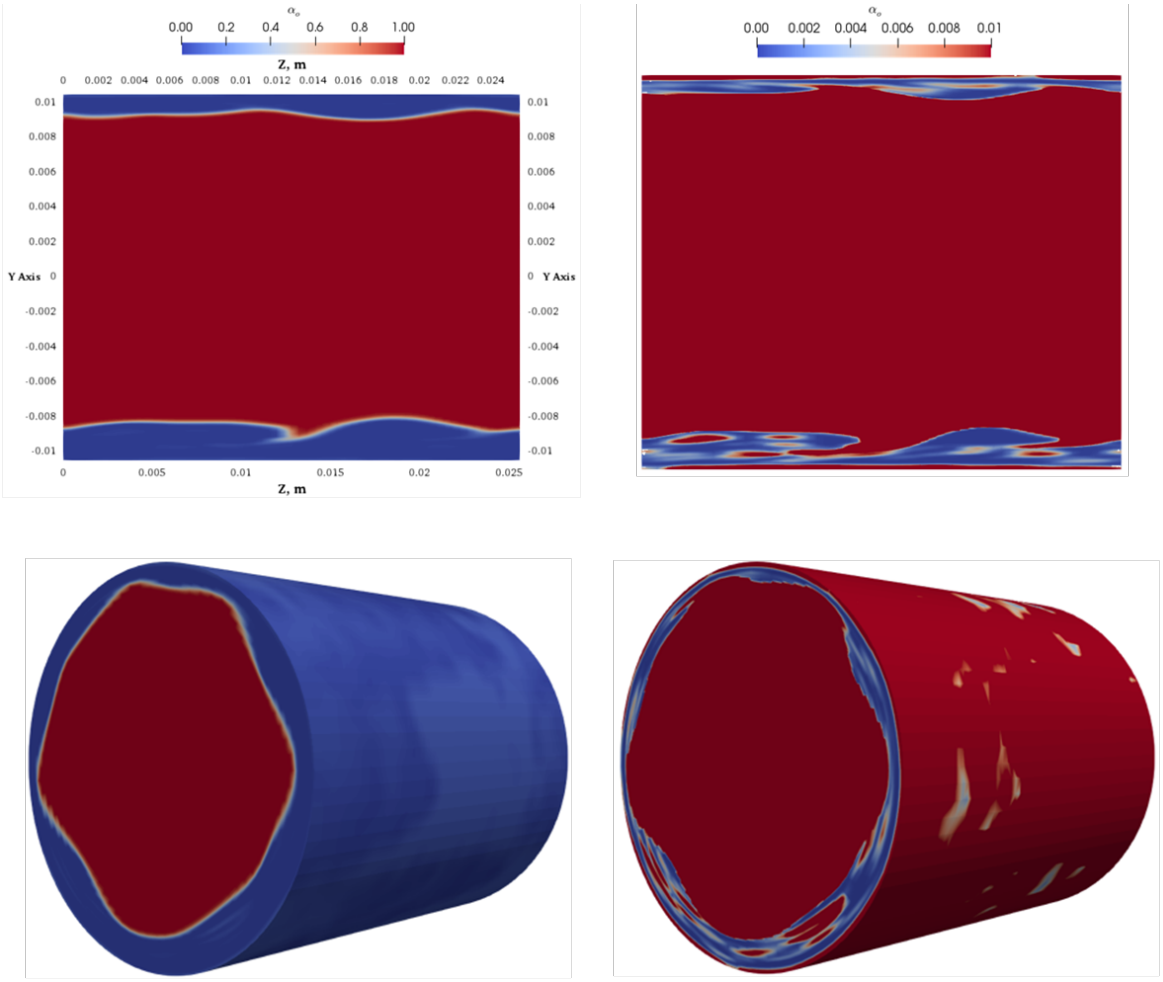

(a) Color map range: $0 < \alpha_o < 1$ **(b)** Color map range: $0 < \alpha_o < 0.01$

Figure 5-2: Color function of the volume fraction with CVOF method at the conditions with T = 40 °C, m = 3093, H = 1.39, Q_a = 0.43 L/s, ε = 20%.

To find the reason for the deviations as described above, we studied the simulation results obtained by Konings in detail, especially the distribution of the oil and water phases. With the application of the color function, the phase interface is still clear and visible with the bare eye, as shown in 5-2(a). Note in this snapshot that there is some slight dispersion of the oil phase in the annulus, which was also detected in the experiments. However, if we change the legend from $0 < \alpha_o < 1$ to $0 < \alpha_o < 0.01$, the noticeable oil dispersion over the whole annulus is found, shown in 5-2(b). Moreover, it seems that the dispersion is more severe at the wall region and around the wave trough than elsewhere. Since the viscosity ratio m is larger than 10^3, the mixture viscosity close to the pipe wall yields that $\nu_m > 11\nu_w$, as shown in figure 5-3. This is leading to a significantly higher wall shear stress at the pipe wall. According to the force balance of the fully-developed periodic flow in the horizontal pipe, the pressure force in the streamwise direction was mainly balanced by the wall shear stress, which was the reason of the over-prediction in the previous research. This oil dispersion, as found in Chapter 4, is highly dependent on the temperature, and has little influence at 20 °C.

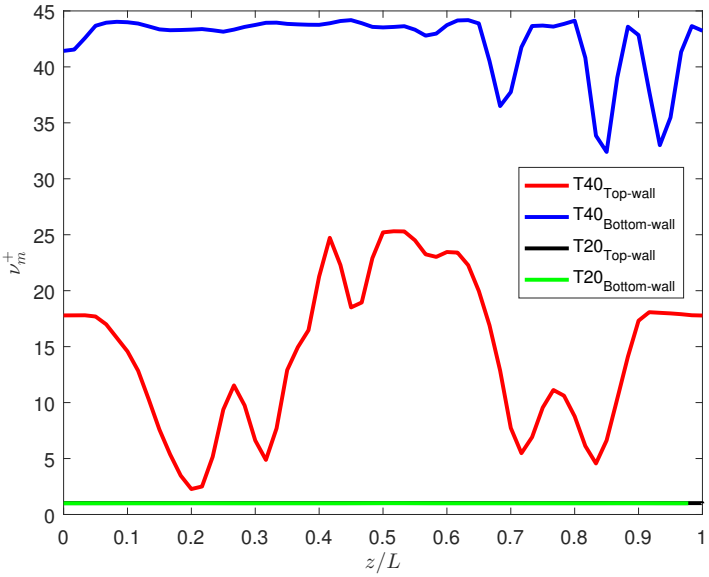

Figure 5-3: Distribution of the dimensionless mixture viscosity ν_m^+ along the streamwise direction on the wall at 20 °C and 40 °C. $\nu_m^+ = \nu_m/\nu_w$, where $\nu_m = \nu_w\alpha_w + \nu_o\alpha_o$, $\nu_w = 9.74\times10^{-7}$ m^2/s, 6.74×10^{-7} m^2/s, respectively.

5-2 3D simulation with the CLSVOF method

5-2-1 Simulation set up

With the pressure-imposed solver, the 3D simulation at the conditions with $T = 40\,°C$, $m = 3093$, $H = 1.39$, $dp/dz = 1100$ Pa/m is carried out with the CLSVOF method in OpenFOAM. As introduced in subsection 3-3-2, this method can alleviate the numerical dispersion between the two immiscible fluids, while maintaining a very good mass conservation. The Launder-Sharma low-Re $k-\epsilon$ turbulence model is still employed.

Consistent with the simulation by Konings (2017), the configuration used for the test is $R_2 = 10.5$ mm, $L = 25.58$ mm, with the mesh revolution of $126\times80\times60$ in the radial, circumferential, and axial direction, respectively. The mesh size close to the wall is also chosen to satisfy that $y^+ < 1$. Since the final volumetric flow rate is supposed to be consistent with the experimental data (see 5-1), the initial flow field is set up as PCAF with $R_1 = 9.04$ mm, here R_1 is calculated from equation 4-5. During the simulation, the ratio of V_o to V_w is always a constant as long as the mass conservation is satisfied, leading to the linear correlation between the hold-up ratio and the water-cut. The need to specify an a-priori value for H and ε is a drawback of the pressure-imposed solver. The reason why we choose this solver is that the pressure-imposed solver has a much faster convergence speed than the flux-imposed solver.

The discretization schemes and matrix solvers are identical with those of the 2D wedge-shape model. With respect to the Courant number, according to the criteria of equation 4-1 and 4-2, we have chosen $Co = 0.01$ with $\Delta t = 5\times10^{-6}$ s.

For the initialization, the set up of the velocity field and of the volume fraction field follows

equations 4-3 and 4-4. Similarly, the wall boundary conditions for U, ϵ and k are of the Dirichlet type and those for p and α are of the Neumann type.

A sinusoidal perturbation in one wave length is added along the interface to create a wave with an amplitude of 2×10^{-5} m.

5-2-2 Convergence check

The convergence check for the 3D simulation is based on the total upward momentum of the core and on the volumetric flow rates of the two phases, as shown in figure 5-4. The total upward momentum of the core starts to oscillate around 0 within the range of $|M_{o,y}| < 5{\times}10^{-7}$ at $t = 0.6$ s. Similarly, the volumetric flow rates of the two phases, measured at the outlet of pipe, convergence to a constant value at about $t = 1$ s. Although the amplitude and eccentricity are more fluctuating during the simulation, it is shown that these values become relatively stable at about $t = 2$ s. Therefore, the simulation can be concluded to have converged after $t > 2$ s.

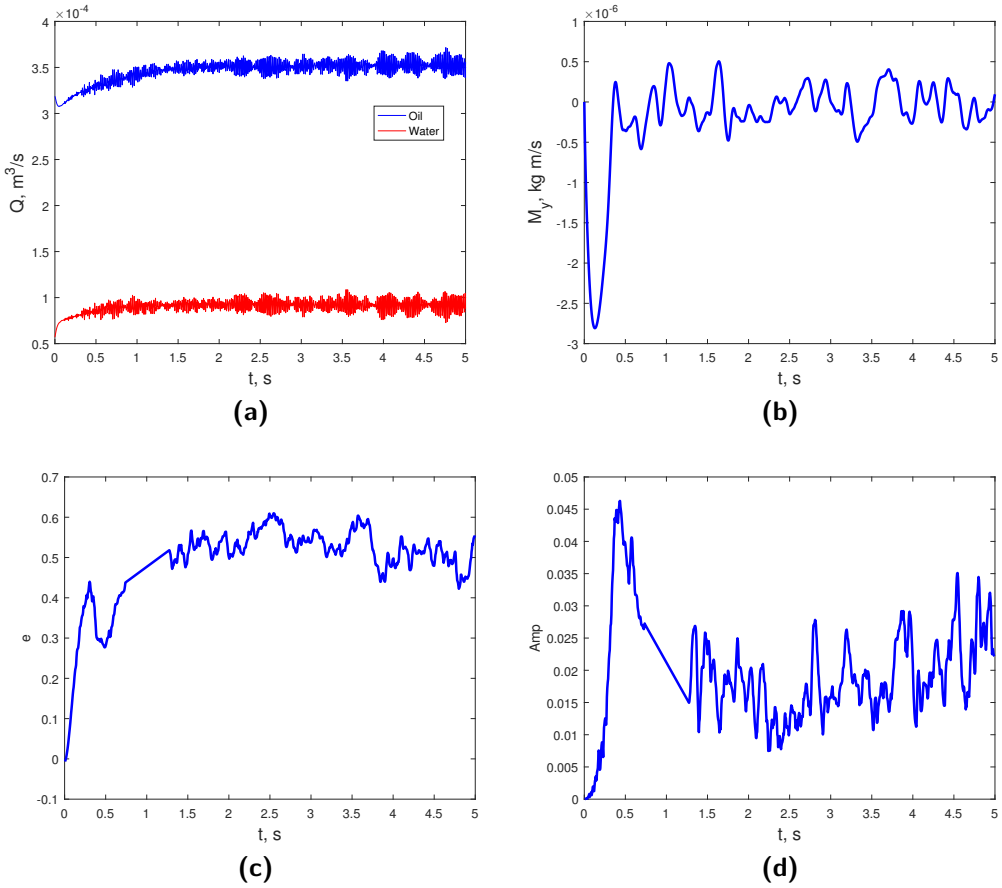

Figure 5-4: Convergence check for the 3D simulation with the CLSVOF method at 40 °C. (a) Volumetric flow rate of the two phases as a function of time; (b) Total upward momentum of the core as a function of time; (c) Eccentricity of the core as a function of time; (d) Interface wave amplitude as a function of time.

5-2-3 Comparison with the CVOF case

Figure 5-5 shows the volume fraction distribution over the pipe at $t = 6.79$ s. Similarly, the color map is compared with two different legends. In this snapshot, the eccentricity seems to be a bit larger than in the CVOF case while the core-annular flow pattern remains valid. The phase interface at the bottom is also slightly blurred in figure 5-5a, because of the coarse grid around the interface region. Furthermore, in figure 5-5b, the dispersion of the oil phase is found to be still present in the water annulus, but it is significantly alleviated close to the wall region. This will also contribute to the lower wall shear stress, which is in line with the lower pressure gradient.

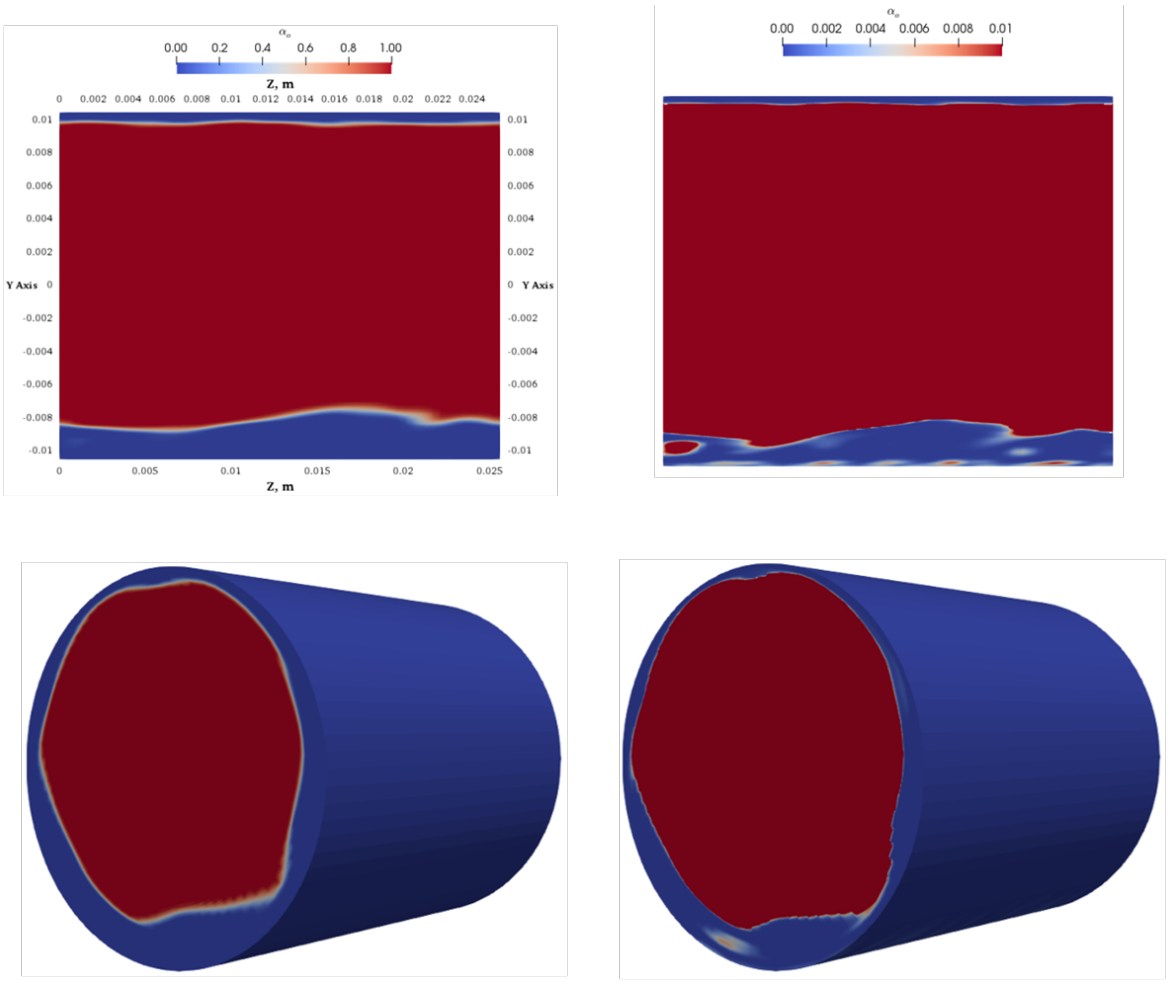

(a) Color map range: $0 < \alpha_o < 1$ **(b)** Color map range: $0 < \alpha_o < 0.01$

Figure 5-5: Color function of the volume fraction with the CLSVOF method at the conditions with $T = 40\,^{\circ}\mathrm{C}$, $m = 3093$, $H = 1.39$, $dp/dz = 1100$ Pa

The dimensionless mixture viscosity is shown again for the CLSVOF case in figure 5-6. The value of ν_m^+ decreases significantly, especially at the top wall. The numerical dispersion of the oil phase almost disappears at the top wall while ν_m^+ at the bottom wall is still larger than

1. Notice that the fluid property ν_m is not identical at the inlet and at the outlet, which is in contradiction with the periodic boundary condition. This may be due to the round-off error in the linear interpolation. The distance from the '$\alpha_o = 0.5$' iso-line to the bound of the interface region is still visible, which means that several layers of cells are still present in the interface region. To conclude, it was shown that the CLSVOF method is able to successfully alleviate the numerical dispersion of the oil phase in the water annulus, while there is no significant improvement of the sharpness of the interface.

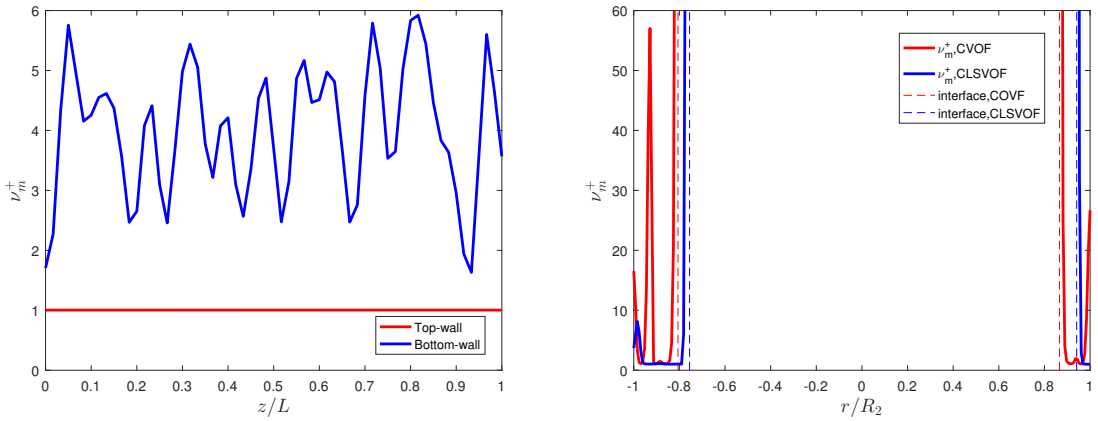

Figure 5-6: Dimensionless mixture viscosity ν_m^+ distribution for: (a) the CLSVOF case along the streamwise direction on the wall, (b) the CLSVOF and CVOF cases along the radial direction at $z/L = 0.5$ line, at 40 °C. The dashed line is the interface defined as $\alpha_o = 0.5$. $\nu_w = 6.74\times10^{-7}$ m^2/s.

As mentioned before, the numerical dispersion is supposed to be the primary cause of the over-prediction of the pressure gradient in the CVOF case. To demonstrate this, the averaged flow characteristics e.g. the water-cut ε, the volumetric flow rate, the eccentricity e and the wave amplitude A_{top} are listed in table 5-1.

Table 5-1: Simulation results for the CVOF case and for the CLSVOF case compared to the experimental data at 40 °C

Case	$Q_o[m^3/s]$	$Q_w[m^3/s]$	$\Delta p[Pa/m]$	$\varepsilon[\%]$	e	A_{top}	$\gamma[\%]$
CVOF	36.5×10^{-5}	7.3×10^{-5}	2830	16.7	0.18	0.042	0.32
CLSVOF	35.0×10^{-5}	9.2×10^{-5}	1100	20.1	0.51	0.021	0.84
Experiment	34.5×10^{-5}	8.6×10^{-5}	1086	20.0	/	/	/

It is found that the CLSVOF case shows good agreement with the experimental data. With the imposed pressure gradient of $dp/dz = 1100$ Pa/m, the differences in the oil flow rate and in the water flow rate are only 1.2 % and 3.7 %, respectively. That is to say, the over-prediction of the pressure gradient in the CVOF case disappears as well as the under-prediction of water-cut, while a sufficiently accurate mass conservation is achieved.

Apart from the difference in the numerical dispersion, the core is closer to the top wall with a less fluctuating wave in the CLSVOF case. The flow visualization by Konings (2017) has shown that at the same water-cut, the eccentricity increases with a decrease in the water viscosity (giving a lower Reynolds number in the water annulus). Furthermore, in the turbulent numerical simulation by Huang et al. (1994), it was also found that at the same hold-up ratio, the friction factor was higher due to the increase in the eccentricity. All of the cases mentioned in the previous research, and also including our case, have a turbulent water annulus, in which the Reynolds number is always higher than the threshold value as proposed by Bai et al. (1996) and Ooms et al. (2013). This leads to the 'flying core flow' interpretation: in the core-annular flow with a difference between the water and oil density, the core tends to be lifted due to the buoyancy force while the rising of it would squeeze the water close to the top wall and relax the water on the bottom. During the rising process, the pressure distribution over the narrow part of the annulus will be intensified, generating a downward pressure force, which counterbalances the buoyancy force. The pressure force increases as the annulus on the top becomes thinner. Therefore, for the CLSVOF case with a lower pressure gradient, the core has to levitate more eccentrically to maintain a sufficiently large pressure force. This also explains why the eccentricity increases with a dcreasing friction factor and with an increasing temperature (lower water viscosity) in the high-Reynolds number region. Figure 5-7 shows the distribution of the reduced pressure p_r (which is the pressure without the contribution of the gravity) for the two models, here $p_r = p - \rho g h$. As discussed in Ooms et al. (2013), the pressure in front of the wave crest is expected to be higher than that at the bottom. For our cases, the streamwise distribution of the normal component of the pressure over interface is shown in figure 5-8. Note that the reduced pressure includes the pressure gradient along the streamwise direction. On average, the reduced pressure on the top interface is higher than that on the bottom interface for both cases with a difference of 6.4 Pa and 8.4 Pa, verifying the "flying-core" interpretation.

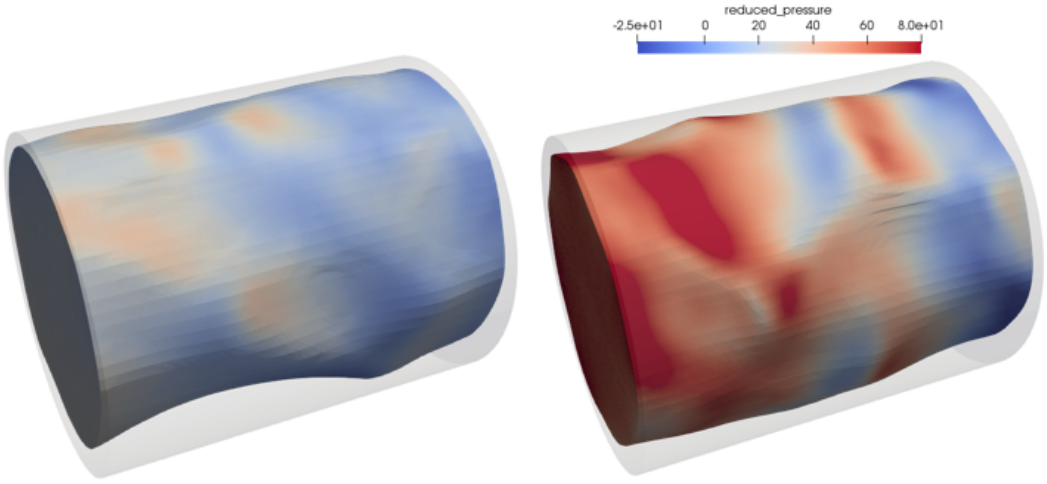

(a) CLSVOF **(b)** CVOF

Figure 5-7: Distribution of the reduced pressure (pressure without gravity contribution) over the core for the CLSVOF case and for the CVOF case

Moreover, as the final vertical pressure force should be mainly counterbalanced by the buoy-

ancy force on the core (the contribution of the normal component of the viscous force at the interface is small), and as the buoyancy force is identical in the two cases, the vertical component of interface normal vector should be lower than that for the CLSVOF case. This is consistent with the difference in amplitude listed in table 5-1; the CVOF case has a more rippling interface than the CLSVOF case.

Besides this, the narrow gap between the core and the top wall will restrict the growth of the wave amplitude, which prevents fouling. This also explains why the amplitude in the CLSVOF case is smaller.

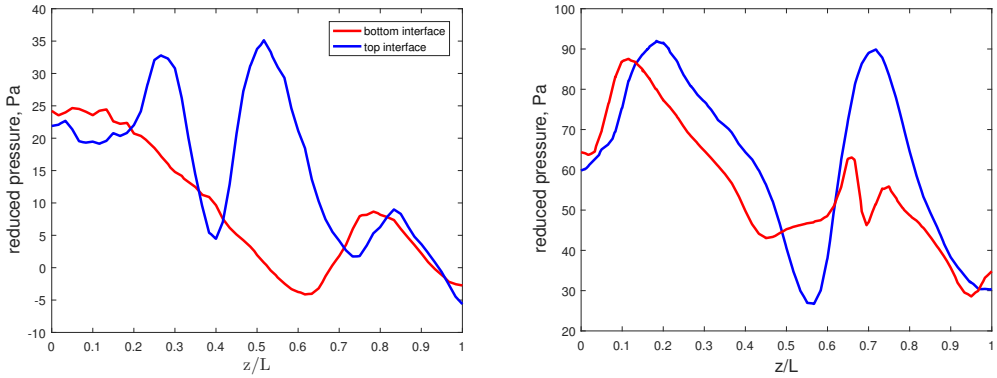

(a) CLSVOF **(b)** CVOF

Figure 5-8: Distribution of the reduced pressure (pressure without gravity contribution) along the interface for the CLSVOF case and for the CVOF case; blue line = top interface, and red line = bottom interface

The water-lubricated flow requires pressures comparable to pumping water alone at the same throughput. The single-phase water simulation with the same pressure gradient shows a strong turbulence in the pipe centre, i.e. ν_t^+ is larger than 90. Therefore it is worthwhile to investigate the turbulence distribution in the water annulus. Figure 5-9 compares several turbulent parameters in the CVOF and CLSVOF cases, as well as the velocity field and the volume fraction distribution along the vertical line through the pipe centre at the inlet cross section. All these quantities are nondimensionalized by the procedures applied in Chapter 4.

On the whole, both the CLSVOF and CVOF simulations show a strong turbulence in the water annulus with a maximum in ν_t+ of 45 and 20, respectively. The Reynolds number in the annulus is $Re_a = (\sqrt{R_2^2 - R_c^2}\bar{u}_w/\nu_w) = 7724, 6357$, respectively, which gives flow in the turbulence region. Here $R_c = 1/2\sqrt{V_c/L\pi}$ is the volume-equivalent radius of the core. The flow parameters have more symmetric patterns in the CVOF case due to the smaller eccentricity. A low oil fraction in a small part of the wall region in the CLSVOF case is still found while the influence on the lubrication transport is evident. Due to the improvement in the oil dispersion, the irregular perturbation of the turbulence parameters disappears in the vertical direction. The increase of the eccentricity intensifies the nonuniform distribution in the top annulus and in the bottom annulus.

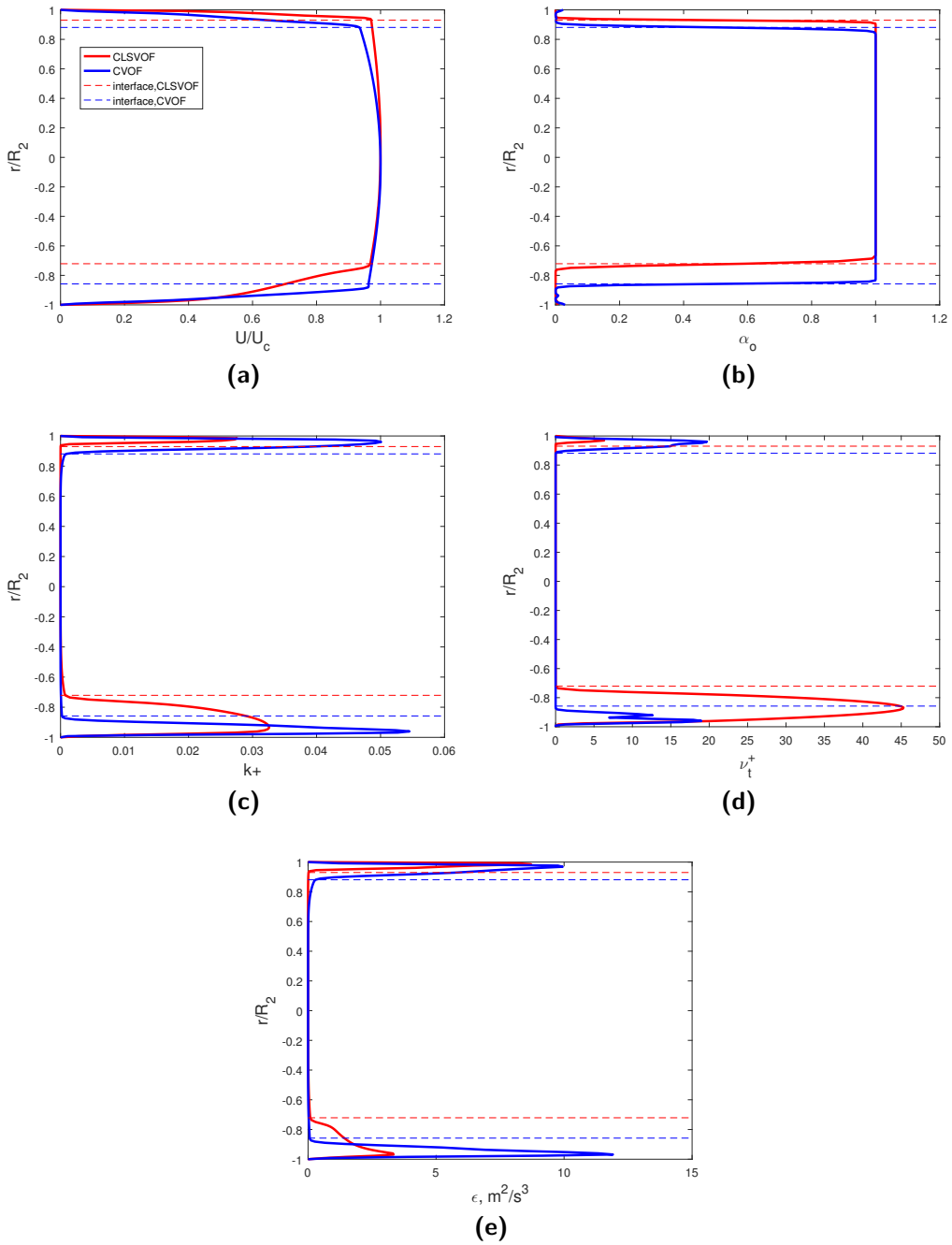

Figure 5-9: Dimensionless velocity, volume fraction, turbulence kinetic energy, eddy viscosity and turbulence dissipation distribution along the vertical line through the pipe center at the inlet cross section, here $k^+ = k/\bar{U}_a^2$,$\bar{U}_a$ is the averaged velocity in the annulus, Red: CLSVOF, blue: CVOF

Generally, in both cases, the peak value of the turbulence kinetic energy is not sensitive to the core position while the eddy viscosity decreases significantly as the annulus becomes thinner. In the $k-\epsilon$ turbulence model, the eddy viscosity is proportional to the square of the kinetic

energy and inversely proportional to the dissipation rate as,

$$\nu_t = c_\mu \frac{k^2}{\epsilon}, \tag{5-5}$$

here c_μ is the constant in $k-\epsilon$ turbulence model. According to equation 5-5, the higher turbulence dissipation is expected in the narrow top annulus compared to the bottom annulus. This is also consistent with the scaling analysis of the turbulence dissipation:

$$\epsilon = \mathcal{O}(\frac{\mathcal{U}^3}{\mathcal{L}}), \tag{5-6}$$

where $\mathcal{U}$ and $\mathcal{L}$ are the characteristics velocity and length scale in the annulus, chosen as $\bar{U}_a$ and the averaged annulus height $\bar{h}_a$, respectively. Similarly, according to equation 5-6, ϵ is also larger in the top annulus, validating the turbulence distribution in the two cases. This all means that the thicker annulus and the lower mixture viscosity boost the turbulence generation process in the annulus in the CLSVOF case while the unpredictable oil dispersion would increase the peak value of the turbulent kinetic energy in the CVOF case.

5-3 20% water-cut at different temperatures

In this section simulations are carried out with CLSVOF method at different temperatures with $T = 20\,^\circ\text{C}, 30\,^\circ\text{C}, 50\,^\circ\text{C}$ in 3D multiphase simulations, and also with $40\,^\circ\text{C}$ as already discussed before. The new simulation results will be compared with the experimental data by Duin (2016) and with the simulations by Konings (2017). The pressure-imposed solver with $dp/dz = 1100$ Pa/m, $H = 1.39$ is still applied in the same computational domain. The properties of the two fluids at different temperature are listed below:

Temperature [°C]	m	a	ξ
20	3072	0.86	0.914
30	1745	0.86	0.910
40	1148	0.86	0.908
50	746	0.86	0.905

5-3-1 Convergence check and fouling

Although the experiments by Duin (2016) have shown that many oil droplets are formed at the interface and entrained into the water annulus at $50\,^\circ\text{C}$, the pressure drop of that flow was measured to be consistent with that at a lower temperature, indicating the core-annular flow pattern was still held at this temperature. In contrast to the experiments, the core-annular flow pattern remains valid for the low temperature cases with the CLSVOF method while fouling occurs at $T = 50\,^\circ\text{C}$, as shown in figure 5-10. This fouling phenomenon was also found in the simulation of Konings (2017) with the CVOF method. The interface becomes blurred and loses the sinusoidal shape. Severe oil dispersion reappears at the wall region,

which results in a plunge of the velocity field close to the top wall. At the same time, the Couette-type water flow in the bottom annulus decelerates due to the low transport velocity of the core and at the wave interface. Besides this, the absence of oil droplets in the water annulus would be mainly caused by the limitation of the grid scale.

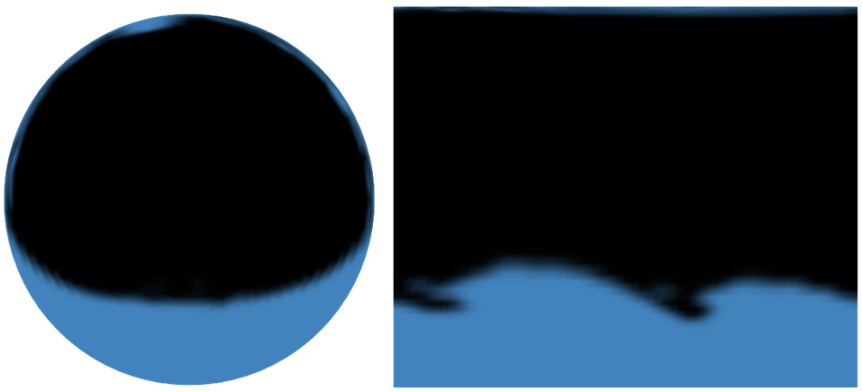

(a) (b)

Figure 5-10: Fouling occurs at $T = 50\,^{\circ}\mathrm{C}$ close to the top wall

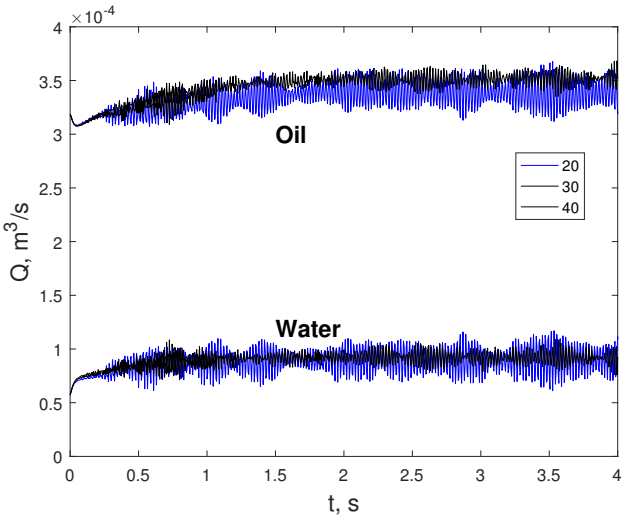

Figure 5-11: Oil flow rate and water flow rate as function of time at $20\,^{\circ}\mathrm{C}$, $30\,^{\circ}\mathrm{C}$, $40\,^{\circ}\mathrm{C}$

It was found in the previous research by Konings. that the eccentricity increased with the temperature at the same water-cut and at the same pressure gradient, due to the decrease of the water viscosity. During the rising of the core, the pressure force that is generated in downward direction is not sufficiently large to maintain the levitation until the wave crest starts to touch the top wall. The turbulence model fails and the wall shear stress increases dramatically once the fouling starts.

In contrast to the CVOF simulation in which the whole transition from fouling to stratified flow could be simulated, the simulation with the CLSVOF method fails during the

re-initialization process once the fouling is apparent at the top wall, shown in figure 5-10. Theoretically, the level set function is calculated as the signed normal distance to the nearest reconstructed interface. However, during the re-initialization of it, the severe change in the interface topology close to the wall region, like the formation of small oil droplets, introduces a difficulty to evaluate the interface grid. Consequently, the interface transition regions overlap with each other, leading to the collapse of the re-initialization process. Generally, the demonstration of the fouling tendency in the CLSVOF case is consistent with the CVOF case.

Considering the volumetric flow rate, the simulations reach a stable state within $t = 2$ s for termperature of 20, 30, 40 °C, shown in figure 5-11. Although the additional re-initialization procedure has to be executed in the simulation with the CLSVOF method, the convergence speed of it at 20 °C is only slightly slower than that of the CVOF case, namely by about 6 %. Moreover, due to the irregular distribution of the viscosity over the annulus, which aggravates the condition of the coefficient matrix during the pressure-velocity coupling solution process, the convergence speed of the CVOF case at 40 °C is even much slower than that of the CLSVOF case. The ratio of t_c/t in the former one can increase to 3 times of that in latter one with the same Courant number and Δt; here t_c is the accumulated CPU time.

5-3-2 Results comparison

Similar to the results described in subsection 5-2-3, the time-averaged flow parameters are listed and compared with the experimental data in table 5-2. With the imposed pressure gradient, the predicted oil flow rate V_o is almost identical to the experimental value and the difference of V_w is only around 5%, which shows that the prediction is quite accurate. The result at 40 °C is added to the water-cut / flow-rate chart created by Konings in figure 5-12. Due to time limitation of this project, the rest of the cases have not been repeated with the new method. A better prediction, however, is expected with CLSVOF method also for the other conditions in the figure.

Table 5-2: Simulation results of the CVOF case and of the CLSVOF case, compared to the experimental data at 20 °C, 30 °C and 40 °C

Temperature	Case	$Q_o[m^3/s]$	$Q_w[m^3/s]$	$\Delta p[Pa/m]$	$\varepsilon[\%]$	$\gamma[\%]$
20	CLSVOF	34.0×10^{-5}	9.1×10^{-5}	1100	21.1	0.30
	Experiment	34.5×10^{-5}	8.6×10^{-5}	1004	20.0	/
	CVOF	34.5×10^{-5}	8.6×10^{-5}	951	19.9	0.16
30	CLSVOF	34.5×10^{-5}	9.1×10^{-5}	1100	21.0	0.20
	Experiment	34.5×10^{-5}	8.6×10^{-5}	1084	20.0	/
	CVOF	34.7×10^{-5}	8.3×10^{-5}	1215	19.2	0.18
40	CLSVOF	35.0×10^{-5}	9.1×10^{-5}	1100	20.1	0.84
	Experiment	34.5×10^{-5}	8.6×10^{-5}	1086	20.0	/
	CVOF	36.5×10^{-5}	7.3×10^{-5}	2830	16.7	0.32

Except for fouling, the CLSVOF method has been proven to be a reliable interface capturing method, which gives a good prediction of the flow rate with a reasonable computational expense, not only in the high temperature range (i.e. lower oil viscosities), but also in the low temperature range (i.e. higher oil viscosities). Concerning the mass conservation, the error in the volume fraction only slightly increases with the temperature as long as the core-annular flow is maintained while a significant mass loss is found at 50 °C where there is fouling that gives stratified flow. The error in the volume fraction is much larger in the CLSVOF case, namely 7.7%, than that in CVOF case, 2.7%, which is due to the shortcoming in the use of the level set function. This function is known to suffer from mass loss in the high-curvature or poorly resolved region, which is formed due to the fouling of the wall.

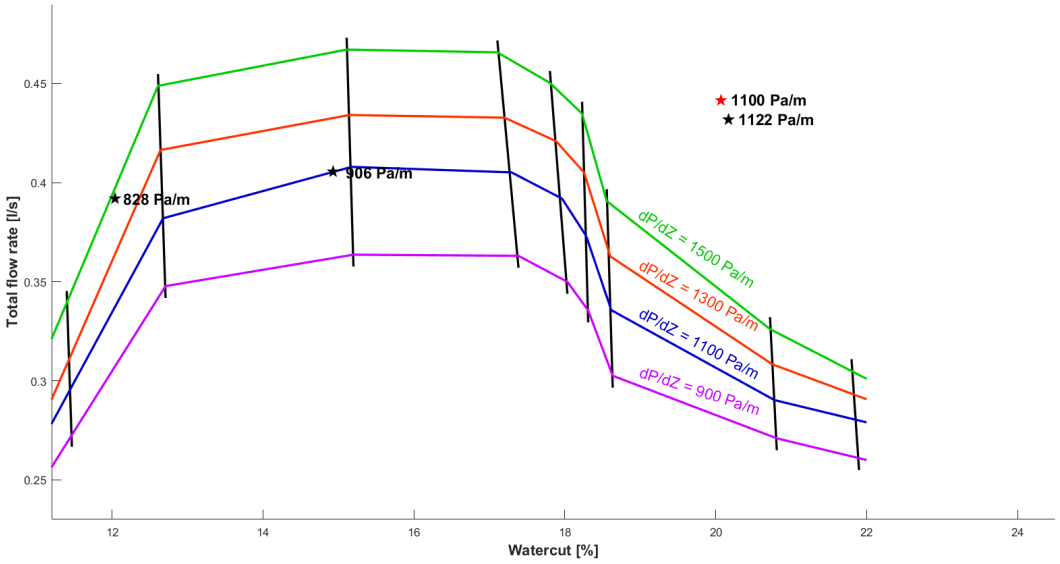

Figure 5-12: Water-cut and total flow rate results for the different holdup fractions (black lines) and pressure gradients (colored lines) with the VOF method and the extra case with the CLSVOF method at 40 °C. Black stars: experimental data, red star: results of the CLSVOF method; modified from the figure by Konings (2017)

The flow field of the three temperatures are investigated thoroughly. Figure 5-13 shows the contours of the instantaneous streamwise velocity relative to the core velocity for $T = 20, 30, 40\,^{\circ}\mathrm{C}$ on the bottom half of the pipe. Here the core velocity is chosen as the averaged velocity of the core, $\bar{u}_{core} = \int u dV_c / V_c$, V_c is the volume of the core. Apart from the region around the wave trough, the core region shows an almost plug-flow pattern, with the velocity of $u_c = 1.328, 1.344, 1, 345\mathrm{m/s}$, respectively. The decrease of the oil viscosity due to the increase of the temperature reduces the uniformity of the velocity over the core region, which reflects the nature of the viscosity: the resistance to a gradual deformation by shear stress. As the temperature increases, the phase interface gradually loses the sinusoidal shape, which is accompanied by the secondary wave and by an increase of the wave number. Furthermore, due to the decrease of the viscosity of water, the time-averaged wave amplitude decreases from $A_{top} = 0.0539$, 0.0409 to 0.0221, while the eccentricity increases from $e = 0.0615$, 0.285 to 0.491, respectively. This variation of the amplitude and eccentricity is similar to the finding

in section 5-2, where the liquid in the annulus for the CVOF case can be treated as liquid with a higher kinematic viscosity than that of water.

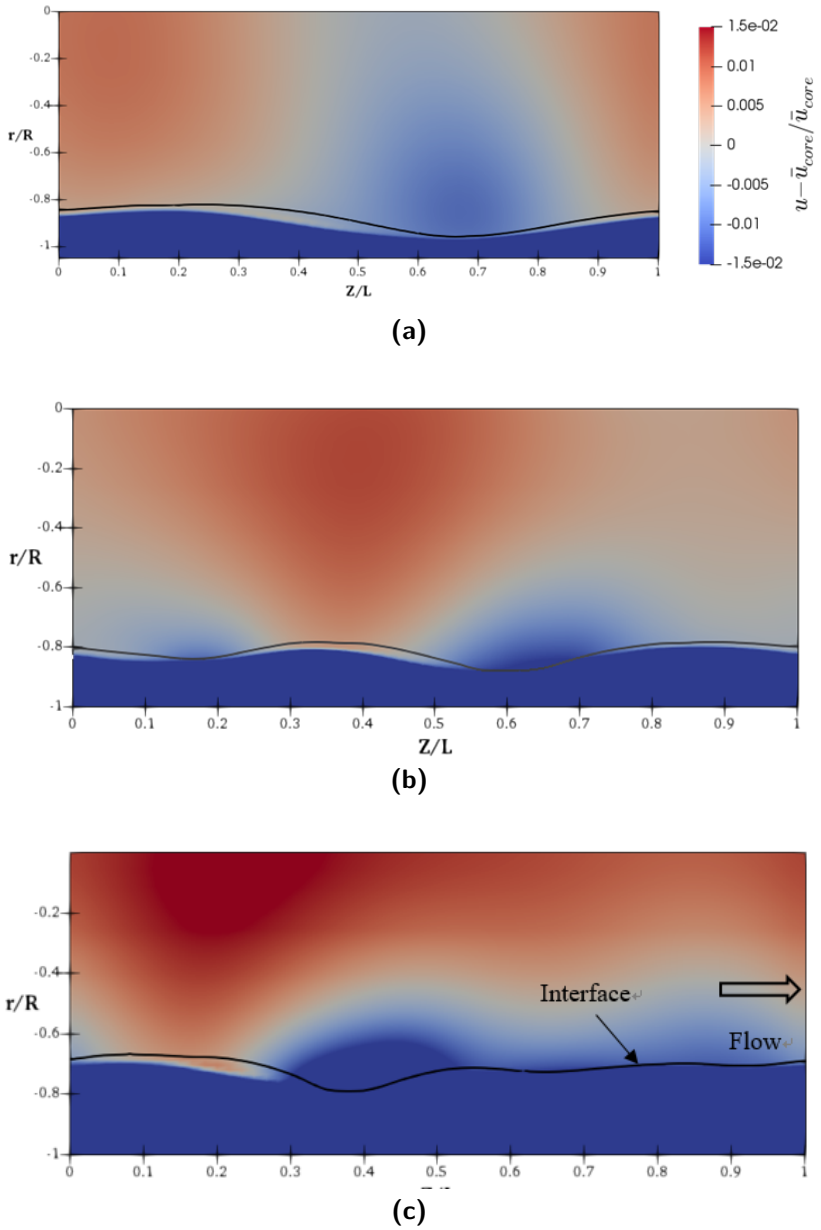

Figure 5-13: Contours of the instantaneous streamwise velocity relative to the core velocity: (a) $T = 20\,^{\circ}\mathrm{C}$,(b) $T = 30\,^{\circ}\mathrm{C}$,(c) $T = 40\,^{\circ}\mathrm{C}$. The black line denotes the phase interface

The pressure force works on the oil core as well as the buoyancy force. These forces are integrated in the vertical direction, averaged in time and listed in table 5-3. Here the shear force is calculated from the force balance in the vertical direction, while including the momentum of the core in vertical direction $M_c, y \approx 0$:

$$F_{s,y} + F_{b,y} = F_{p,y}, \tag{5-7}$$

Table 5-3: Time-averaged force in the vertical direction exerted on the core

Temperature $[°C]$	$F_{p,y}$ $[N]$	$F_{b,y}$ $[N]$	$F_{s,y}$ $[N]$	$\Delta\rho$ $[kg/m^3]$
20	5.916×10^{-3}	5.524×10^{-3}	3.89×10^{-4}	86
30	5.874×10^{-3}	5.749×10^{-3}	1.26×10^{-4}	89
40	5.829×10^{-3}	5.954×10^{-3}	1.25×10^{-4}	92

where $F_{s,y}, F_{b,y}, F_{p,y}$ denote the shear force, buoyancy force, and pressure force in vertical direction, respectively, and $\Delta\rho = \rho_w - \rho_o$. The buoyancy force, as shown in the table, slightly increases with temperature due to the small increase of the density difference. Accordingly, the contribution of the shear stress in the vertical direction also increases. Consistent with the decrease in the wave fluctuation, the actual magnitude of the shear force has increased.

In addition, the friction factor is calculated to check the applicability of the lubrication transport technique. It is defined in (M. S. Arney and Liu, 1993) as:

$$\lambda = \frac{8\tau_w}{\rho\bar{u}^2}, \tag{5-8}$$

here τ_w is the wall shear stress, N/m^2, and $\bar{u}_s$ is the overall superficial velocity calculated as $\bar{u}_s = (\bar{Q}_o + \bar{Q}_w)/\pi R_2^2$.

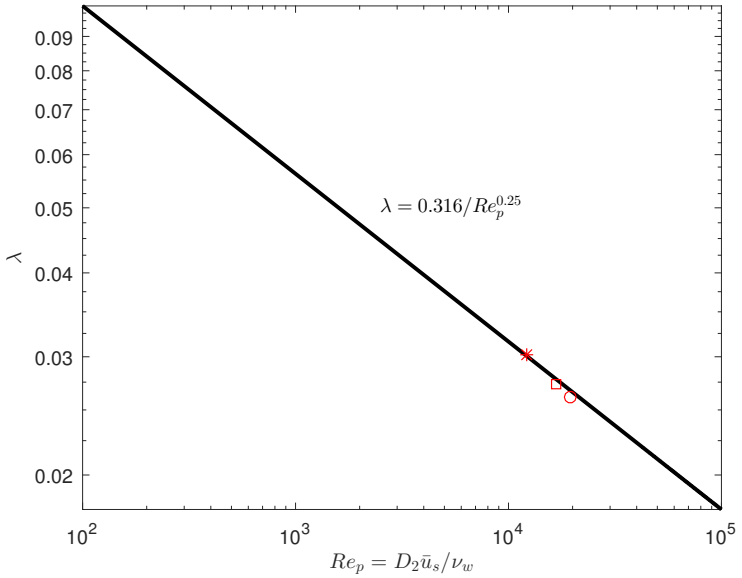

Figure 5-14: Friction factor of the simulation at $T = 20, 30, 40\,°\mathrm{C}$ with the CLSVOF method as compared to the Blasius correlation for turbulent flow, here D_2 is the diameter of the pipe: Asterisk, $20\,°\mathrm{C}$, Square, $30\,°\mathrm{C}$, Circle, $40\,°\mathrm{C}$.

The averaged value of the friction factor is interpolated and compared with the Blasius correlation for turbulent flow in figure 5-14. The lubrication transport of the core-annular flow reduces the friction factor to almost the same magnitude as found for the single-phase water

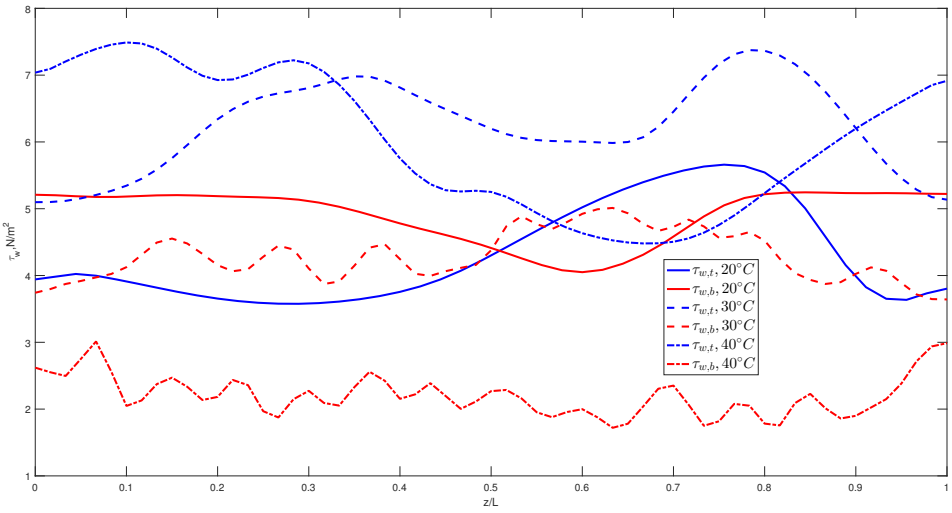

Figure 5-15: Distribution of the instantaneous wall shear stress τ_w along the top wall and along the bottom wall at different temperatures: —, 20 °C,−−, 30 °C, .−, 40 °C, blue, top wall, red, bottom wall

flow in the high turbulence region, $Re_p > 10000$. The friction factor, similar to the water flow in the pipe, decreases as the temperature increases, which is due to the decrease of the water viscosity. Investigating the distribution of the shear stress, it is found that the top wall contributes to the friction force most, as is shown in figure 5-15. On average, the difference between the top wall shear stress and the bottom wall shear stress shows a positive correlation with the eccentricity. As the top part of the annulus decreases, the flow between the interface and the wall is sometimes limited to the inertial sublayer (or to the logarithmic layer). Due to the lack of data for the the flow profile of the Couette type in the annulus, we take the classical turbulent pipe flow as a reference. Based on the Prandtl mixing length hypothesis, we choose two cross sections, namely one at the top wave peak and one at the top wave valley, in the simulation for $T = 40\,°\mathrm{C}$, plot the velocity field in the vertical direction and compare them with the classical linear profile in the viscous sublayer and with the logarithmic profile in the inertial sublayer of the turbulent channel flow. The two correlations are formulated as follows:

$$u^+ = \begin{cases} y+, & 0 < y^+ < 10 \\ \frac{1}{k} \ln y^+ + 5.5, & y^+ > 10 \end{cases} \tag{5-9}$$

here $u^+ = u/u_\tau, y^+ = yu_\tau/\nu$, and $u_\tau = \sqrt{\tau_w/\rho}$ as based on the wall shear stress. An analogy can be made with the logarithmic layer at $y^+ = 300$ for the fully-developed wall-bounded turbulent flow with a Reynolds number of about 10000 (Den Toonder and Nieuwstadt, 1997). It is shown in figure 5-16 that the flow in narrowest part of the top annulus (blue open circles) is still in the logarithmic layer. Here the height of the gap is so narrow that the generation of concentrated turbulent kinetic energy must be compensated by the high dissipation in the energy cascade process, which leads to the large velocity gradient close to wall in the top annulus. This is the reason that the difference in the wall shear stress between the top wall and bottom wall increases with the eccentricity.

As for the thicker annulus (red data), the velocity field close to the interface deviates from the logarithmic profile, which is acceptable as the the driving force of the flow in the annulus is not only the pressure gradient, but also the shear stress from the moving wave. In Chapter 4 we discussed the similarity of the interface to the solid wavy wall at a different temperature; it is shown in figure 4-12 that the magnitude of the viscous stress around the interface is smaller than that of the wall-bounded flow at $T = 40\,^{\circ}\mathrm{C}$. Intuitively, the oil core is expected to act more like a solid core for the lower temperature, where the oil viscosity is higher. Therefore, we divide the flow field in the annulus into two parts, based on the distance to the wall and to the interface. The flow in the lower part close to the wall is nondimensionalized with the wall shear stress and the flow in the upper part close to the interface is nondimensionalized with the viscous stress at the interface. Note that due to the presence of the transition region around the interface, the shear stress calculated at the location with the level that was set to zero is not reliable, and we thus need to use the Fanning friction factor as calculated by the Blasius correlation based on the relative Reynolds number to the interface, defined as $Re_r = (u_{wave} - \bar{u})h/\nu_w$. Accordingly, the shear stress can be calculated with equation 5-8 and the frictional velocity at interface can be calculated as $u_{\tau,int} = \sqrt{\tau_{int}/\rho_w}$.

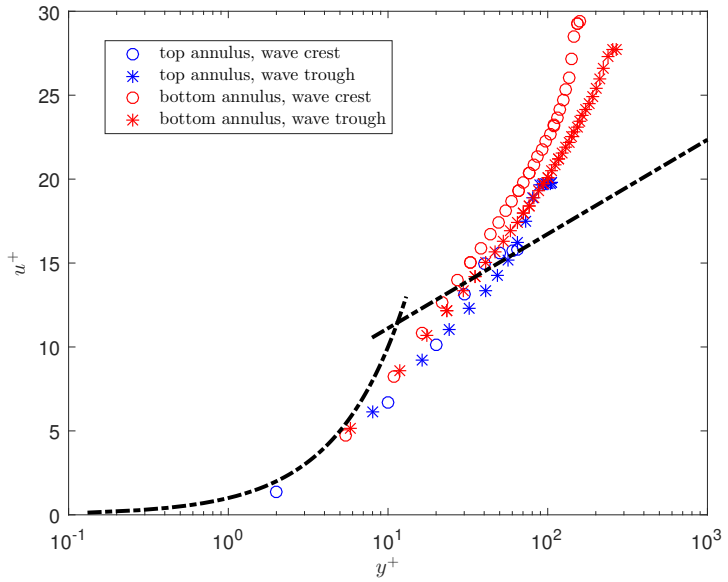

Figure 5-16: Dimensionless velocity profile u^+ (based on wall shear stress) as a function of the dimensionless wall distance y^+ for the turbulent flow between the pipe wall and the interface with $Re_a = \bar{u}_a\bar{h}/\nu_w$ around 7×10^3 at $T = 40\,^{\circ}\mathrm{C}$, here $\bar{u}_a$ is the average velocity in the annulus and $\bar{h}$ is the average annulus height. The dashed line denotes the linear profile and the logarithmic profile from equation 5-9. Blue refers to data in the top annulus, and red refers to data in the bottom annulus. The asterisk $*$ refers to data in the wave valley, and open symbols to data in the wave peak

Following the nondimensionalization procedure introduced above, figure 5-17 shows the re-organized data profile at $T = 40\,^{\circ}\mathrm{C}$ and at $20\,^{\circ}\mathrm{C}$. In both cases, the flow close to the interface deviates from the theoretical profile, indicating that the interface does not act like a wall in the 3D simulation. The deviation is more distinct in $40\,^{\circ}\mathrm{C}$, verifying that the solid-

core assumption of the interface is more appropriate for the flow at the lower temperature. Furthermore, as the flow profile close to the interface is more like a linear profile, one possible reason for the deviation is that the dimensionless numbers employed by equation 5-9 are all calculated based on the water viscosity, which is still not completely equal to the mixture viscosity below the interface. Therefore, the actual $y^+ = yu_\tau/\nu_m$ should be smaller than used in the profile, leading to the left shift of the data with the blue symbol. Also as shown in figure 5-16, the y^+ value of the first cell is larger than 5 in the wave valley. Since the velocity field of the first cell is assumed to be fully resolved, it would lead to an inaccuracy in the wall region. A higher grid resolution, especially close to wall and interface, is recommended for use in further research.

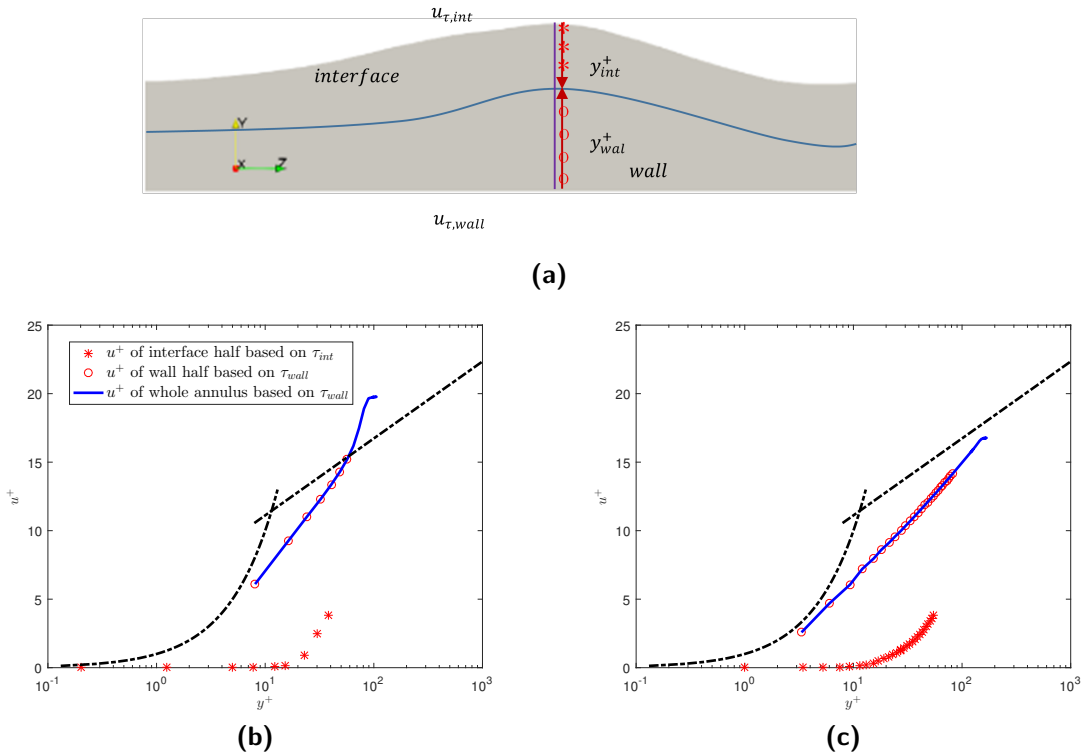

Figure 5-17: Dimensionless velocity profile u^+ (based on the wall shear stress or on the interface viscous stress) as a function of the dimensionless wall/interface distance y^+ for turbulent flow in the annulus.(a), sketch map of the nondimensionlization process, (b), flow at $40\,^{\circ}\mathrm{C}$,(c), flow at $20\,^{\circ}\mathrm{C}$. Red asterisk $*$, flow close to the wall, blue open symbols o, flow close to the interface, solid line $--$, interpolation of data based on τ_w

5-4 Convergence study of the CLSVOF method

The convergence study for the model with the CLSVOF interface capturing method is performed in this section. The simulations are carried out for the vertical core-annular flow in the wedge-shaped domain with the geometry of 4.75×11.6 mm and a grid of 128×128 cells in the radial and streamwise directions. The length of it is the same as the fastest growing disturbance wavelength, according to the linear stability analysis conducted by Li and Renardy

(1999). Statistically, the flow is in the laminar region at the conditions listed below:

$$m = 602, \quad a = 1.28, \quad \xi = 0.909, \quad K = -0.454, \quad J = 7.96e-2, \quad Re_1 = 0.95, \tag{5-10}$$

where K is the ratio of the driving force in the core and in the annulus and J is the surface tension parameter, formulated as:

$$K = \frac{dp/dz + \rho_o g}{dp/dz + \rho_w g}, \quad J = \frac{\sigma R_1 \rho_o}{\mu_o^2}. \tag{5-11}$$

Comparisons are made with the results from the linear stability analysis and with results from the simulations with the CVOF method as obtained by Beerens et al. (2014). According to the theoretical analysis, the amplitude development follows an exponential pattern:

$$Amp(t) = Amp(0)e^{kt}, \tag{5-12}$$

with the theoretical growth rate $k = 0.1940$ at this condition. Note that k and t have been nondimensionalized as $k = k^* R_1 / V_o^*(0)$ and $t = t^* V_o^* / R_1$, k^* and t^* are the dimensional terms, V_o^* is the initial core velocity and R_1 is the core radius in the PCAF pattern. The simulation is initialized with the sinusoidal perturbation with amplitude $Amp(0) = 10^{-6}$ m.

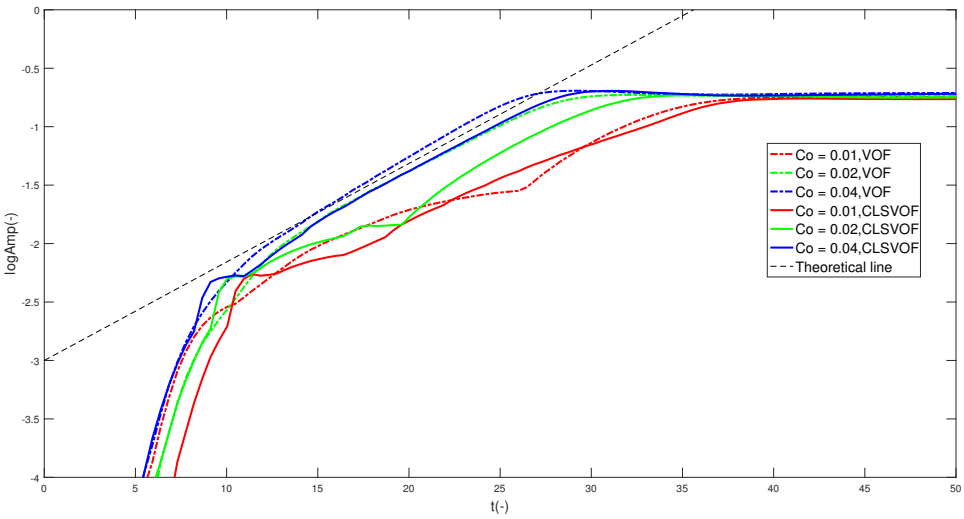

Figure 5-18: Amplitude as function of time in the semi-logarithmic coordinate axis. The simulations are conducted with different Courant numbers using the constant $\Delta t = 1 \times 10^{-6}$: dashed line, theoretical growth rate from the linear stability analysis.

Figure 5-18 shows the growth rate of the simulation with different Courant numbers, here the maximum value of Δt is kept at 1×10^{-6} s. Note that the Courant number and the time step mentioned here are the maximum values set in OpenFOAM, while the actual values of them in every cell vary with the definition of the Courant number according to equation 4-1. For both methods, the simulated growth rate is only similar to the theoretical one at the condition $Co = 0.04$ while the final amplitudes of the waves develop to the same value after convergence in all cases. The simulations with the CLSVOF method show a more oscillating pattern at the

beginning, which becomes even stronger with a decrease of the Courant number. In general, the difference in the computational expense between the two methods appears to be small, due to the weak oil dispersion and the small simulation domain in the 2D model. $Co = 0.04$ is concluded to be the appropriate number from the perspective of the amplitude growth rate for the wedge-shaped model. Further research is recommended for the convergence study of the 3D model.

5-5 Conclusion

The CLSVOF interface capturing method has been proven to be a reliable approach for the prediction of the volumetric flow rate and of the water-cut at different temperatures. The difference in the oil flow rate is almost negligible and the over-prediction in the water flow rate is only by around 5%. Compared to the CVOF method, the CLSVOF method is not able to improve the sharpness of the interface while it can succesfully alleviate the numerical dispersion of the oil phase in the water annulus. The latter prevents the mixture of the two fluids in the wall region, and thus corrects the over-prediction of the pressure gradient in the previous simulation with the CVOF method. On the other hand, the reduction of the oil dispersion accelerates the numerical calculation speed during the pressure-velocity coupling process, leading to an increase of the real time factor (i.e. ratio between the physical simulation time and the CPU time ratio) to 3 at 40 °C.

Futhermore, simulations were carried out at $T = 20, 30, 40, 50\,^{\circ}\text{C}$ (giving a decreasing oil viscosity) and with a similar water-cut. Due to the failure in the re-initialization process, the simulation at 50 °C no longer converges as soon as the stratified flow regime starts to appear due to fouling of the top wall by oil. Apart from this, the core-annular flow regime remains valid in the other cases and the eccentricity of the core increases with the temperature. This increase in eccentricity is found to enlarge the difference in the wall shear stress between the top wall and the bottom wall. In addition, the friction factor of the flow agrees with the Blasius correlation and shows a positive correlation with the viscosity, which confirms the applicability of the lubrication technique. The flow field in the annulus was investigated in detail and it was found that the turbulence model fails in some cross sections due to the limitation in the annulus height. A refined grid around the wall and interface is recommended for further research to fully resolve the flow.

Finally, the convergence study of the CLSVOF method based on the linear stability analysis in the wedge-shaped model is consistent with that of the CVOF method. By studying the computational effort for the case in which the growth rate of the wave amplitude is considered, $Co = 0.04$ is concluded to be the appropriate Courant number for the 2D model. The convergence study for the 3D model is recommended for the further research.

Chapter 6

Conclusions and recommendations

6-1 Conclusions

The interface between oil and water in core-annular flow in a pipeline has been investigated through numerical simulations with three types of models: 3D multiphase flow in a pipe section, 2D multiphase flow in an axi-symmetric pipe section (wedge-shaped section), in which gravity is ignored, and 2D single phase water flow in the annulus, using an imposed wavy boundary. Different temperatures have been simulated, namely 20, 30, 40 and 50 °C, corresponding to an oil viscosity of 3338, 1472, 718, and 383 cSt, respectively. The Launder-Sharma low-Reynolds-number $k-\epsilon$ turbulence model and the Volume of Fluid method were used in the fully-developed transient multiphase simulations with periodic boundary conditions, while the steady state solver was used for the single-phase simulations. The CFD package OpenFOAM was applied for all the simulations.

The wavy interface as found from the 2D axi-symmetric multiphase simulation was used as a boundary in the single-phase model for the water annulus. In these single-phase simulations the wavy-interface was represented by a fixed, stagnant wavy wall, while the pipe wall was moving in opposite direction with the wave velocity. In this way the results for the water annulus as obtained with the 'interface-bounded' approach (in fact the 2D multiphase model) and with the 'wall-bounded' approach (in fact the single-phase model) could be compared. A close similarity was found between the two models for the water annulus: the presence of a recirculation zone around the wave crest (in a reference frame moving with the wave velocity), the adverse pressure gradient in the wave trough, the dependency of the displacement thickness on the annulus height, etc. However, due to the numerical dispersion of some oil in the water annulus introduced by the VOF method in the multiphase model, the turbulence showed a higher level in the results with the single-phase model, while the results with the multiphase model were affected by the unpredictable distribution of the mixture viscosity, caused by the oil dispersion. On the other hand, the water flow in the annulus was of the Couette type, which gives a high dependency of the water flow rate on the shear stress imposed by the moving interface wave. Therefore, the macroscopic flow field in the two models was quite similar. Note that the oil dispersion in the 2D multiphase model for the annulus

could probably have been prevented by using the Coupled Level Set and Volume of Fluid method, instead of the VoF method, but this was not verified in the present study.

In an effort to resolve the deviation with the experimental value of the pressure drop at 40 ^{o} (718 cSt oil viscosity) as found in the 3D multiphase flow simulation with the VOF method, we implemented the Coupled Level Set and Volume of Fluid (CLSVOF) method based on the Compressive Volume of Fluid method in OpenFOAM. The deviation was expected to be due to dispersion of oil in the water annulus, which is of numerical nature induced by the VOF method. The 3D transient simulations were carried out in the horizontal pipe with the interFOAM solver. Indeed it was found that the CLSVOF method did significantly reduce the dispersion of oil in the water annulus in the wall region close to the wall. The CLSVOF method, however, did not improve the sharpness of the interface oil/water interface. The introduction of the level set function provided a more accurate representation of the vector normal to the interface, which improves the accuracy of the surface tension term in the momentum equations. The simulation results carried out with the CLSVOF method showed a good agreement with the experimental data performed in previous research. The largest difference in the water flow rate was only 5% and the convergence speed at 40 °C (718 cSt oil viscosity) increased by a factor 2. Consequently, the CLSVOF method was concluded to be a reliable interface capturing method with an acceptable computational expense for the prediction of oil/water core-annular flow.

The turbulent water flow in the annulus was investigated at various temperatures (i.e. with various oil viscosities). The fouling occurred close to the top-wall at 50% during the simulation, mainly caused by the failure of the re-initialization process for the level set function. At the other temperatures, the water-lubricated transport showed a similar friction factor as for the single phase pipe flow, verifying the applicability of the core-annular flow in a wide temperature range. The levitation model in high-Reynolds number flow has been verified to be valid for different temperatures (oil and water viscosities) while the net pressure force in the vertical direction decreased as the temperature increased at the same throughput. The eccentricity of the core was found to increase with temperature which caused a larger difference between the wall shear stresses at the top and bottom walls.

A convergence study of the CLSVOF method was carried out in the 2D wedge-shaped model in the vertical pipe, at the same input conditions as used in the linear stability analysis performed by Li and Renardy (1999). The growth rate of amplitude as function of time was compared with constant time step and different Courant number. The simulation with the CLSVOF method generated more oscillations during the development of the wave amplitude, which was even more aggravated when the Courant number was decreased. Finally, $\mathrm{Co} = 0.04$ was found to give an amplitude growth in the 2D simulation that is similar to the theoretical analysis.

6-2 Recommendations

Although the numerical predictions of the core-annular flow in the horizontal pipe were valid up to some engineering level, the turbulence details in the water annulus have not been thoroughly investigated so far. The flow in the first cell of the viscous layer was proven to be not fully resolved, leading to an unreliable prediction of the velocity distribution by the

turbulence model. A refined mesh is recommended with special focus on the wall and interface regions.

Furthermore, as found at various temperatures, the CLSVOF method did not improve the sharpness of the phase i the normal distance from the first $\alpha > 0.999$ cell centre to the first $\alpha < 0.001$ cell centre, we can find that $h_{i,clsvof} = 1.11\times10^{-3}$ m is even slightly larger than $h_{i,cvof} = 6.63\times10^{-4}$ m. As defined in equation 3-15, $h_{i,clsvof}$ is restricted by the pre-defined thickness χ in the regularized Heaviside function while $h_{i,cvof}$ has a close relation with the artificial constant c_α chosen in equation 3-9. Also, $\chi = c_\chi h$ is influenced by the mesh quality around the interface and by the constant c_χ. These two constants, c_α and c_χ, are given the values as suggested in the literature. For a more precise reconstruction of the interface, it is worthwhile to carry out a convergence study for these two constants, with the criteria of the interface thickness.

In addtition, the CLSVOF method is more sensitive to topology changes than the CVOF method in an inertia-dominated flow. The simulation suffered from severe mass fluctuations at 50 °C when fouling occurs at the wall, which is mainly caused by the choice for the interface capturing method. However, it was reported by Deshpande et al. (2012) that the mass conservation performance is better with the CVOF method than with the CLSVOF method in the surface-tension dominated simulation of a 3D droplet in a vortex flow field. Whether the difference is influenced by the value of the Weber number of the droplet is still unclear.

The numerical algorithm of our CLSVOF method is different from the first version proposed by Sussman and Puckett (2000), although both the LS and VOF methods are used. In the formulation by Sussman et al., the advection of the LS function is also solved. The coupling between α and Φ is achieved through a spatial integral of the Heaviside function, which is shown in Appendix A. The simplification of the LS advection in our method speeds up the simulation. It is recommended to make a comparison with CLSVOF method of Sussman et al. to check the influence of the level set advection, especially with respect to the performance of the mass conservation.

It is recommended to repeat the 2D multiphase simulations in the annulus, which so far were only carried out with the VOF method, also with the CLSVOF method. This will probably mitigate the oil dispersion in the water annulus, and thus will enable to carry out a better comparison between the annulus results as obtained with the 2D multiphase model and with the single-phase model.

It is also recommended to carry out a systematic study of the predictions for the pressure gradient and the holdup for a range of oil and water flowrates at 40 °C and at other temperatures.The results can be compared with engineering models and correlations, such as the one for core-annular flow as proposed by Ullmann and Brauner (2004).

Appendix A

Coupled Level Set and Volume of Fluid Method with two-way coupling

We consider a grid cell Ω with a volume ΔV in the computational domain. The volume fraction can be related to the LS function as:

$$\alpha_\Omega = \frac{1}{\Delta V}\int_\Omega H(\Phi)dxdydz \tag{A-1}$$

The coupled second-order operator in the split algorithm proposed by Puckett et al. (1997) is used to implement the advection of $\alpha^n_{i,j,k}$ and $\Phi^n_{i,j,k}$ as:

$$\bar{s}_{i,j,k} = \frac{s^n_{i,j,k} + (\Delta t/\Delta x)(G_{i-1/2,j,k} - G_{i+1/2,j,k})}{1-(\Delta t/\Delta x)(u_{i+1/2,j,k} - u_{i-1/2,j,k})}, \tag{A-2}$$

$$\hat{s}_{i,j,k} = \frac{\bar{s}_{i,j,k} + (\Delta t/\Delta y)(G_{i,j-1/2,k} - G_{i,j+1/2,k})}{1-(\Delta t/\Delta y)(u_{i,j+1/2,k} - u_{i,j-1/2,k})}, \tag{A-3}$$

$$\tilde{s}_{i,j,k} = \frac{\hat{s}_{i,j,k} + (\Delta t/\Delta z)(G_{i,j,k-1/2} - G_{i,j,k+1/2})}{1-(\Delta t/\Delta z)(u_{i,j,k+1/2} - u_{i,j,k-1/2})}, \tag{A-4}$$

$$\begin{aligned} s^{n+1}_{i,j,k} = \bar{s} - \Delta t[&\frac{\tilde{s}}{\Delta x}(u_{i+1/2,j,k} - u_{i-1/2,j,k}) + \frac{\hat{s}}{\Delta y}(v_{i,j+1/2,k} - v_{i,j-1/2,k}) \\ &+\frac{\bar{s}}{\Delta z}(w_{i,j,k+1/2} - w_{i,j,k-1/2})], \end{aligned} \tag{A-5}$$

here s represents the level set function Φ and the volume fraction α, $G_{i-1/2,j,k} = s_{i+1/2,j}u_{i+1/2,j}$ denotes the surface flux of s across the left edge of the cell and $G_{i,j-1/2,k}, G_{i,j,k-1/2}$ represent the fluxes across the bottom edge and back edge, respectively. The arrangement of the field discretization and of the surface fluxes are illustrated in figure A-1. The interpolation at the

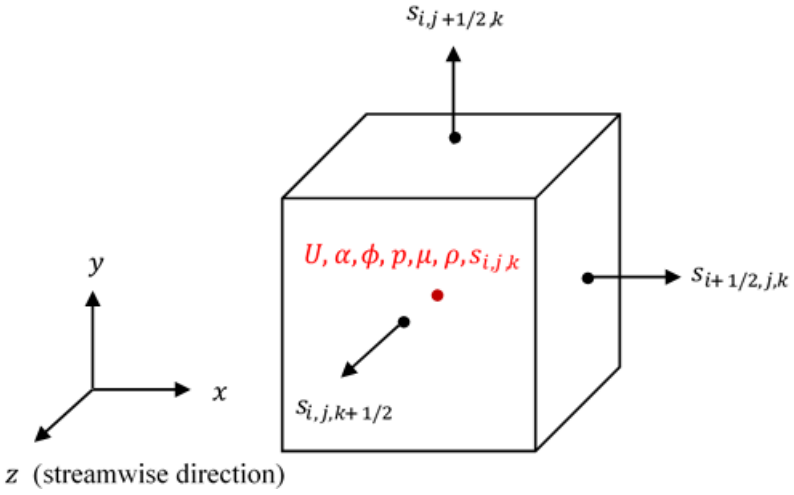

Figure A-1: Advection scheme in a single cell; all the data are stored in the cell centre with the collocated grid

surface is different for α and Φ; taking $\bar{s}_{i+1/2,j,k}$ as a reference gives:

$$\bar{s}_{i+1/2,j,k} = \begin{cases} \bar{s}_{i,j} + \frac{\Delta x}{2}(1 - u_{i+1/2,j,k}\frac{\Delta t}{\Delta x})\frac{\bar{s}_{i+1,j,k} - \bar{s}_{i-1,j,k}}{\Delta x}, & s = \alpha, u_{i+1/2,j,k} > 0 \\ \bar{s}_{i,j} - \frac{\Delta x}{2}(1 + u_{i+1/2,j,k}\frac{\Delta t}{\Delta x})\frac{\bar{s}_{i+2,j,k} - \bar{s}_{i,j,k}}{\Delta x}, & s = \alpha, u_{i+1/2,j,k} < 0 \\ \frac{[\int_{x_{i+1/2}-u_{i,j+1/2}\Delta t}^{x_{i+1/2}} \int_{y_{i+1/2}}^{y_{i-1/2}} \int_{z_{i+1/2}}^{z_{i-1/2}} H(\bar{\Phi}^R_{i,j,k}(x,y,z))dxdydz]}{u_{i+1/2,j,k}\Delta t \Delta y \Delta z} & s = \Phi, u_{i+1/2,j,k} > 0 \\ \frac{[\int_{x_{i+1/2}-u_{i,j+1/2}\Delta t}^{x_{i+1/2}} \int_{y_{i+1/2}}^{y_{i-1/2}} \int_{z_{i+1/2}}^{z_{i-1/2}} H(\bar{\Phi}^R_{i,j,k}(x,y,z))dxdydz]}{u_{i+1/2,j,k}\Delta t \Delta y \Delta z} & s = \Phi, u_{i+1/2,j,k} < 0 \end{cases} \tag{A-6}$$

The advection of the volume fraction is now represented as the co-advected LS function. Here $\bar{\Phi}^R_{i,j,k}(x,y,z)$ is the linear reconstructed interface for the cell $\Omega(i,j,k)$

$$\bar{\Phi}^{R,n}_{i,j,k} = \bar{a}_{i,j,k}(x - x_i) + \bar{b}_{i,j,k}(y - y_j) + \bar{c}_{i,j,k}(z - z_k) + \bar{d}_{i,j,k}, \tag{A-7}$$

Here the superscript n denotes the simulation at time step n. The error in the interface reconstruction is then defined as:

$$E_{i,j,k} = \int_{x_{i-1/2}}^{x_{i+1/2}} \int_{y_{j-1/2}}^{y_{j+1/2}} \int_{z_{k-1/2}}^{z_{k+1/2}} \delta(\Phi)(\Phi - \bar{\Phi}^{R,n}_{i,j,k})^2 dxdydz, \tag{A-8}$$

This can also be written in the following discretized form:

$$E_{i,j,k} = \sum_{i'=i-1}^{i'=i+1} \sum_{j'=j-1}^{i'=j+1} \sum_{k'=k-1}^{k'=k+1} w_{i'-i,j'-j,k'-k}\delta_\epsilon(\Phi_{i',j',k'})(\Phi_{i',j',k'} - \bar{\Phi}^{R,n}_{i',j',k'})^2, \tag{A-9}$$

where $w_{i'-i,j'-j,k'-k}$ is the discrete weight that is equal to 16 for $i = j = k = 0$ and equal to 1 for $i \neq 0$ or $j \neq 0$ or $k \neq 0$, as suggested by Sussman and Puckett (2000). The minimum in the error can be obtained as:

$$\frac{\partial E_{i,j,k}}{\partial a_{i,j,k}} = \frac{\partial E_{i,j,k}}{\partial b_{i,j,k}} = \frac{\partial E_{i,j,k}}{\partial c_{i,j,k}} = \frac{\partial E_{i,j,k}}{\partial d_{i,j,k}} = 0 \tag{A-10}$$

By solving the system matrix for the minimum error, we can reconstruct the phase interface for every cell. After that, the LS function is reinitialized and the coupling process between α and Φ is completed for a single time step. The discretization of the α and Φ advection is not given here. Additional details can be found in Sussman and Puckett (2000).

Bibliography

Bai, R., K. Chen, and D. D. Joseph
1992. Lubricated pipelining: stability of core—annular flow. part 5. experiments and comparison with theory. *Journal of Fluid Mechanics*, 240:97.

Bai, R., K. Kelkar, and D. D. Joseph
1996. Direct simulation of interfacial waves in a high-viscosity-ratio and axisymmetric core–annular flow. *Journal of Fluid Mechanics*, 327:1–37.

Beerens, J. C., G. Ooms, M. J. B. M. Pourquie, and J. Westerweel
2014. A comparison between numerical predictions and theoretical and experimental results for laminar core-annular flow. *AIChE Journal*, 60(8):3046–3056.

Brackbill, J., D. Kothe, and C. Zemach
1992. A continuum method for modeling surface tension. *Journal of Computational Physics*, 100(2):335–354.

Brennen, C. E.
2005. *Fundamentals of Multiphase Flow*. Cambridge: Cambridge University Press.

Chang, Y. C., T. Y. Hou, B. Merriman, and S. Osher
1996. A level set formulation of eulerian interface capturing methods for incompressible fluid flows. *Journal of Computational Physics*, 124(2):449–464.

Den Toonder, J. M. J. and F. T. M. Nieuwstadt
1997. Reynolds number effects in a turbulent pipe flow for low to moderate re. *Physics of Fluids*, 9(11):3398–3409.

Deshpande, S. S., L. Anumolu, and M. F. Trujillo
2012. Evaluating the performance of the two-phase flow solver interfoam. *Computational Science & Discovery*, 5(1):014016.

Duin, E. V.
2016. Influence of oil viscosity on oil-water core-annular flow through a horizontal pipe. Master's thesis, Delft University of Technology.

Feng, J., P. Y. Huang, and D. D. Joseph
1995. Dynamic simulation of the motion of capsules in pipelines. *Journal of Fluid Mechanics*, 286(1):201.

Henrik Rusche
2002. *Computational Fluid Dynamics of Dispersed Two-Phase Flows at High Phase Fractions*. PhD thesis.

Huang, C.Christodoulou, and D.D.Joseph
1994. Friction fractor and holdup studies for lubricated pipelining-ii: Laminar and k-ϵ models of eccentric core flow. *International Journal of Multiphase Flow*, 20:481–491.

Ingen Housz, E., G. Ooms, R. Henkes, M. Pourquie, A. Kidess, and R. Radhakrishnan
2017. A comparison between numerical predictions and experimental results for horizontal core-annular flow with a turbulent annulus. *International Journal of Multiphase Flow*, 95:271–282.

Ismail, A. S. I., I. Ismail, M. Zoveidavianpoor, R. Mohsin, A. Piroozian, M. S. Misnan, and M. Z. Sariman
2015. Review of oil–water through pipes. *Flow Measurement and Instrumentation*, 45:357–374.

Joseph, D. D., R. Bai, K. P. Chen, and Y. Y. Renardy
1997. Core-annular flows. *Annual Review of Fluid Mechanics*, 29(1):65–90.

Joseph, D. D., M. Renardy, and Y. RENARDY
1984. Instability of the flow of two immiscible liquids with different viscosities in a pipe. *Journal of Fluid Mechanics*, 141:309–317.

Kim, K. and H. Choi
2018. Direct numerical simulation of a turbulent core-annular flow with water-lubricated high viscosity oil in a vertical pipe. *Journal of Fluid Mechanics*, 849:419–447.

Ko, T., H. G. Choi, R. Bai, and D. D. Joseph
2002. Finite element method simulation of turbulent wavy core–annular flows using a k–w turbulence model method. *International Journal of Multiphase Flow*, 28(7):1205–1222.

Konings, S. A.
2017. Numerical simulations of core-annular flow through a horizontal pipe. Master's thesis, Delft University of Technology.

Kouris, J. T.
2001. Core-annular flow in a periodically constricted circular tube. part 1. steady-state, linear stability and energy analysis. *Journal of Fluid Mechanics*, 432:181–222.

Launder, B.
1974. Application of the energy-dissipation model of turbulence to the calculation of flow near a spinning disc. *International Communications in Heat and Mass Transfer*, 1(2):131–137.

Li, J. and Y. Renardy
1999. Direct simulation of unsteady axisymmetric core–annular flow with high viscosity ratio. *Journal of Fluid Mechanics*, 391:123–149.

M. S. Arney, R. Bai, E. G. D. D. J. and K. Liu
1993. Friction factor and holdup studies for lubricated pipelining–i: Experiments and correlations. *International Journal of Multiphase Flow*, 19:1061–1076.

Nieuwstadt, F. T. M., B. J. Boersma, and J. Westerweel
2016. *Turbulence: Introduction to theory and applications of turbulent flows*. Cham: Springer.

Ooms, G., M. J. B. M. Pourquie, and J. C. Beerens
2013. On the levitation force in horizontal core-annular flow with a large viscosity ratio and small density ratio. *Physics of Fluids*, 25(3):032102.

Ooms, G., A. Segal, and A. J. van der Wees
1984. A theoretical model for core-annular flow of a very viscous oil coreand a water annulus through a horizontal pipe. *International Journal of Multiphase Flow*, 10:41–60.

Ooms, G., C. Vuik, and P. Poesio
2007. Core-annular flow through a horizontal pipe: Hydrodynamic counterbalancing of buoyancy force on core. *Physics of Fluids*, 19(9):092103.

Polderman, H. G., G. Velraeds, and W. Knol
1986. Turbulent lubrication flow in an annular channel. *Journal of Fluids Engineering*, 108(2):185.

Puckett, Elbridge, G., A. S. Almgren, J. B. Bell, D. L. Marcus, and W. J. Rider
1997. A high-order projection method for tracking fluid interfaces in variable density incompressible flows. *Journal of Computational Physics*, 130(2):269–282.

Renardy, Y. and M. Renardy
2002. Prost: A parabolic reconstruction of surface tension for the volume-of-fluid method. *Journal of Computational Physics*, 183(2):400–421.

Rhoheth Radhakrishnan
2016. The effects of viscosity on core-annular flow. Master's thesis, Delft University of Technology.

Saniere, A., I. Hénaut, and J. F. Argillier
2004. Pipeline transportation of heavy oils, a strategic, economic and technological challenge. *Oil & Gas Science and Technology*, 59(5):455–466.

Shi, J., M. Gourma, and H. Yeung
2017. Cfd simulation of horizontal oil-water flow with matched density and medium viscosity ratio in different flow regimes. *Journal of Petroleum Science and Engineering*, 151:373–383.

Sussman, M. and E. G. Puckett
2000. A coupled level set and volume-of-fluid method for computing 3d and axisymmetric incompressible two-phase flows. *Journal of Computational Physics*, 162(2):301–337.

Sussman, M., P. Smereka, and S. Osher
1994. A level set approach for computing solutions to incompressible two-phase flow. *Journal of Computational Physics*, 114(1):146–159.

Ullmann, A. and N. Brauner
2004. Closure relations for the shear stress in two-fluid models for core annular flow. *Multiphase Science and Technology*, 16:335–387.

Van Der Pijl, A. Segal, C. Vuik and P. Wesseling
2005. A mass-conserving level-set method for modelling of multi-phase flows. *Int. J. Numer. Meth. Fluids*, 47:331–361.

Weller, H. G., G. Tabor, H. Jasak, and C. Fureby
1998. A tensorial approach to computational continuum mechanics using object-oriented techniques. *Computers in Physics*, 12(6):620.

Wilcox, D. C.
1993. *Turbulence Modeling for CFD*. La Canada, CA,: DCW Industries, Inc.

Nomenclature

α	Oil volume fraction	[-]
ϵ	Turbulent dissipation rate	$[m^2/s^3]$
ε	Water cut	[-]
ν	Kinematic viscosity	$[m^2/s]$
ν_t	Eddy viscosity	$[m^2/s]$
ν_m	Mixture viscosity	$[m^2/s]$
μ	Dynamic viscosity	[kgm/s]
ρ	Density	$[kg/m^3]$
ρ_m	Mixture density	$[kg/m^3]$
σ	Surface tension constant	[N/m]
Φ	Level set function	[-]
χ	Interface region thickness	[m]
ξ	Density ratio	[-]
ω	Specific turbulent dissipation rate	[1/s]
a	Radius ratio	[-]
c	Anticipated wave velocity	[m/s]
c_χ	Constant in Level Set function	[-]
c_α	Constant in Volume of Fluid function	[-]
Co	Courant number	[-]
H	Hold-up ratio	[-]
h	Height	[m]
i	Interface	[-]
k	Turbulent kinetic energy	$[m^2/s^2]$
K	Dimensionless driving force	[-]

L	Pipe length	[m]
m	Viscosity ratio	[-]
o	Oil phase	[-]
P	Pressure gradient	[N/m^3]
Q	Volumetric flow rate	[m^3/s]
Re_a	Reynolds number of annulus	[-]
R_1	Radius of the core in perfect core-annular flow	[m]
R_2	Radius of the pipe	[m]
T	Temperature	[$^\circ C$]
w	Water phase	[-]